6
Analyzed Scenarios

This chapter explains the approach taken for creating a computational model in Abaqus® for a specified casing under various cementing scenarios within a salt formation. First, the approximation method and assumptions are established followed by the analytical solutions, model verification, initial and boundary conditions and lastly, data results.

6.1
Case Study

This research has been motivated by CENPES, who requested to conduct further research on poor cementing within the pre-salt basins using data from the article presented by Poiate et al. (2006). Although the article focuses on an approach for drilling fluids, casing design and drilling strategy, it is a valuable reference, providing a case of a poorly-cemented casing subjected to non-uniform salt loading. Using the finite element software ANVEC, Poiate modeled a cemented intermediate casing at various depths in a simulated salt layer shown in Figure 6-1 in reference to Santos Basin, Brazil. This thesis has its interest upon the particular depth of 4301 m that is composed of tachyhydrite, a highly mobile salt mentioned previously in Chapter 1.3 and is currently the most menacing of all salt types in the Santos Basin (Poiate et al., 2006). Poiate's paper included failure scenarios of a poorly-cemented casing considering 1.5% ovality and having a cement channel (or void column) with sizes of 5%, 10%, 15% and 20% of the annulus. The salt properties used in the model derived from samples from the Northeastern state of Sergipe in Brazil—which experts believe to be representative of the salt in the pre-salt layers—its creep behavior approximated by the constitutive law of double mechanism mentioned in Chapter 3.8.4. Instead of modeling a cement channel, a more realistic approach would be to model the cement having a zone consisting of lower elastic parameters and strength properties. This damaged zone, or cement defect, is modeled having different sizes and geometries for comparison, and is simulated for a period of 28 days, allowing the cement to attain adequate compressive strength. In addition, the effects of casing ovalization and eccentricity are taken into consideration in order to simulate worst-case scenarios. This is the approach taken in this research using Abaqus 6.10 considering a similar setting with the same material properties and constitutive model for the salt rock as proposed by Poiate et al. (2006).

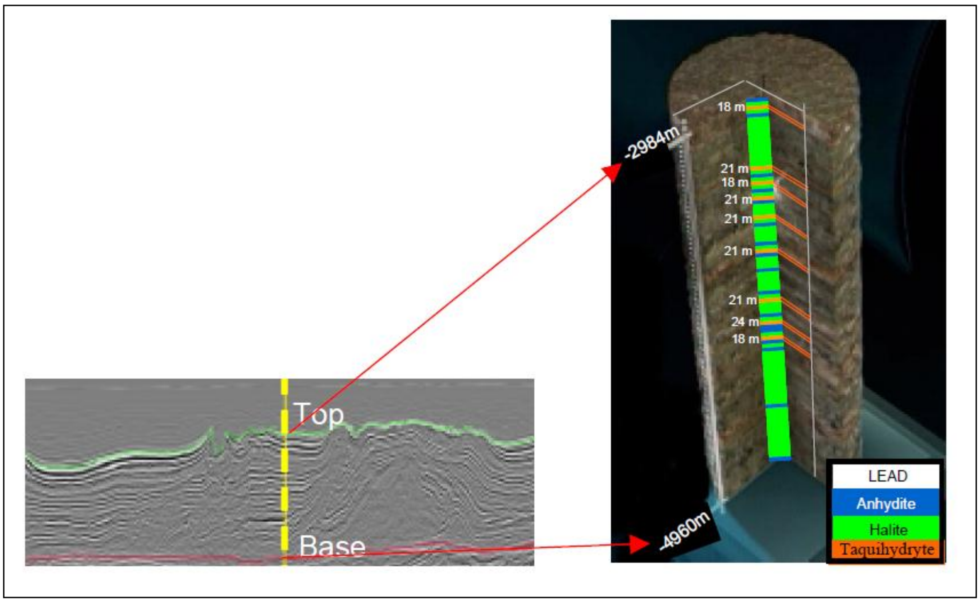

Figure 6-1: Profile and 3D illustration of studied salt sections in Santos Basin, Brazil (Poiate et al., 2006).

6.2
Finite Element Analysis

Seen as the most suitable and appropriate approach, the finite-element analysis method was implemented in this research. The concept behind the finite-element method is approximating the exact solution by taking a given physical model and breaking it down to several pieces and employing a *constitutive law* in numerical methods. A constitutive law is a law that describes the response in a system due to an applied force (Desai, 1979). It should be noted, however, that constitutive laws are not limited to strain and displacement but other laws such as thermal relations—the latter not employed in this thesis. The principles of energy and work are the constitutive laws used to obtain equations that control the element's behavior. A popular example is a vertical load being applied to a free metal plate with only its ends fixed can be approximated by creating small, miniscule pieces (elements) and using a constitutive law where one given element subjected to the load reacts, and its reaction affects the surrounding elements, similar to a “domino effect”. One of the greatest advantages of this method is its capability to be applied to almost *any* sort of physical problem. The elements may be made of any shape or size to mathematically describe the response of the model, allowing the most irregular body shapes to be modeled and approximately solved. Elements are composed of nodes at specified intervals, and their displacements are measured. The unknown variables are solved using matrices along with using initial and boundary conditions. Strictly speaking, finite element analysis determines solutions through the use of matrices, where a matrix is written each for

1. stiffness properties;
2. displacements; and
3. initial and boundary conditions (force, etc.).

Once having the final matrix equation, it is generally solved using linear system solvers. In the finite-element method, there exists convergence requirements that must be satisfied, otherwise the model will yield unreliable results. These can be divided into three groups:

Completeness: The displacement models must include the rigid body displacements and the constant strain states of the element. The elements in the model must approximate well enough so to capture the analytical solution in the event of a mesh refinement process.

Compatibility: The displacements in each element have to correspond with the displacements with the adjacent elements. The shape functions should provide displacement continuity between elements. Physically these behave so that no discontinuities or gaps occur when the elements deform. If the mesh were to be refined, such gaps would make the model worse as they would multiply.

Stability: The system of finite element equations must consistently be approaching the true solution and not diverging from it.

The procedure for finite-element analysis is as follows:

1. Discretize the mass continuum using elements and nodes.
2. Determine the appropriate interpolation polynomial functions and their order.
3. Use the appropriate element type(s) for the model.

4. Define shape function for each element.
5. Define the stress-strain relation.
6. Assemble the element equations to attain the global equations.
7. Solve for the main unknown variables.

It is assumed, however, that the model is continuous, meaning there are no breaks or unconnected points. The method uses *interpolation functions* (or *shape functions*), which describe the shape of the element and the shape it takes when deformed. This work uses lagrangian shape functions, having a value of one at the corresponding node and zero at all other nodes. Shape functions depend on the type of element and its order (linear, quadratic, et al). Consider the linear rectangular element in Figure 6-2, for example: If you substitute the coordinate values of ξ and η for node 1 in the shape function, you will obtain a value of 1. Substituting any other value will give zero.

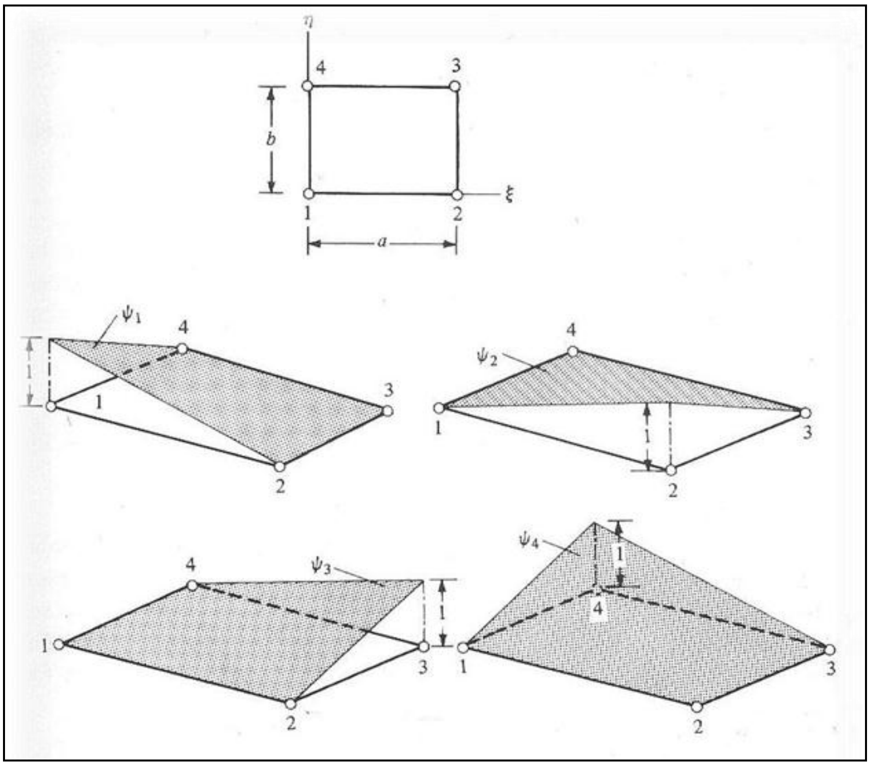

Figure 6-2: Interpolation functions of a four-node rectangular element (Reddy, 1984).

In reference to Figure 6-2, ψ represents the interpolation function, where

$$\psi_1(\xi,\eta) = \left(1 - \frac{\xi}{a}\right)\left(1 - \frac{\eta}{b}\right) \tag{6.1}$$

$$\psi_2(\xi,\eta)=\left(\frac{\xi}{a}\right)\left(1-\frac{\eta}{b}\right) \tag{6.2}$$

$$\psi_3(\xi,\eta)=\frac{\xi}{a}\frac{\eta}{b} \tag{6.3}$$

$$\psi_4(\xi,\eta)=\left(1-\frac{\xi}{a}\right)\frac{\eta}{b} \tag{6.4}$$

It should be noted that in most textbooks, the vector of a shape function is written as $[N]$.

Shape functions are usually written as polynomials because of their easy computation of derivatives, well-balanced functions and low computational effort. Each individual element has its own coordinate system or *local coordinates*. *Lagrangian coordinates* are used in finite element analysis as well as in Abaqus (6.10 Theory Manual 3.2.4). In terms of spatial discretization, the Lagrange method uses a coordinate system (ξ,η) in which its grid moves with the modeled object and is ideal for solid, continuum materials. Another advantage is its computational efficiency. One limitation to the Lagrange spatial discretization is element distortion, where the element can easily become tangled, thus leading to numerical errors (Quan et al., 2003). The order of the polynomial used in the model depends on the modeled topology and on the expected solution nature. In this research, the curved walls of the wellbore, cement and casing along with their inconstant strains indicate that a higher order polynomial should be used to achieve reliable results.

The finite-element method employs a local system and a global system for a given model. The former are coordinates used specifically for the individual element while the latter are coordinates for the model in a "macro" sense. The natural coordinates of the element are commonly written in Lagrangian coordinates (ξ,η) where each range from -1 to +1 in local system and are transformed into cartesian coordinates (x,y). This transformation is done by the use of the *jacobian matrix*. cartesian coordinates, x and y, and natural coordinates, ξ and η, for a quadrilateral element as given in Figure 6-3, may be related as follows

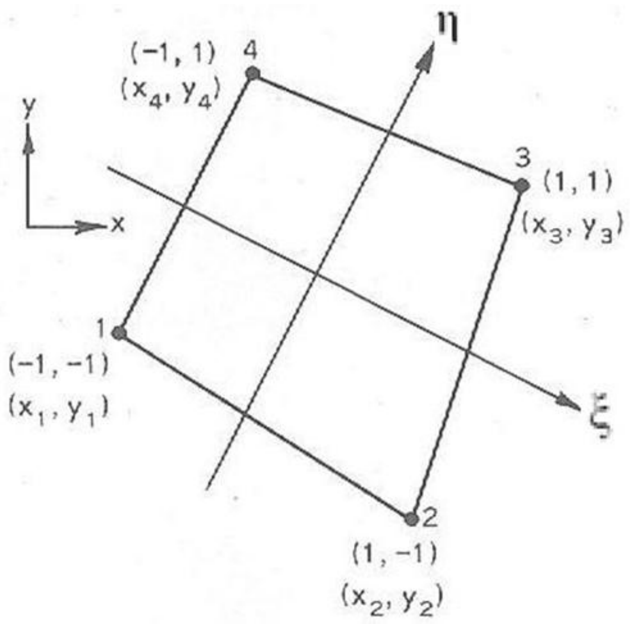

Figure 6-3: Natural and cartesian coordinates on a quadrilateral element. (Desai, 1979 modified).

$$\begin{Bmatrix} x \\ y \end{Bmatrix} = \begin{bmatrix} \{z\}^T & \{0\}^T \\ \{0\}^T & \{z\}^T \end{bmatrix} \begin{Bmatrix} \{x_n\} \\ \{y_n\} \end{Bmatrix} \tag{6.5}$$

Where

$$\{z\}^T = \frac{1}{4}\left[(1-\xi)(1-\eta),(1+\xi)(1-\eta),(1+\xi)(1+\eta),(1-\xi)(1+\eta)\right]$$

$$\{x_n\}^T = [x_1 x_2 x_3 x_4]$$

$$\{y_n\}^T = [y_1 y_2 y_3 y_4]$$

and since the cartesian coordinates for the element must be known, the jacobian operator matrix for this element is written as:

$$\begin{Bmatrix} \dfrac{\partial}{\partial x} \\ \dfrac{\partial}{\partial y} \end{Bmatrix} = [J]^{-1} \begin{Bmatrix} \dfrac{\partial}{\partial \xi} \\ \dfrac{\partial}{\partial \eta} \end{Bmatrix} \tag{6.6}$$

Here, the jacobian matrix $[J]$ is determined from

$$[J]=\begin{bmatrix}\dfrac{\partial}{\partial\xi}\{z\}^T\\ \dfrac{\partial}{\partial\eta}\{z\}^T\end{bmatrix}\left[\{x_n\}\{y_n\}\right] \tag{6.7}$$

and

$$dxdy=\det\left([J]\right)d\xi d\eta \tag{6.8}$$

In order to transform the x and y coordinates into the lagrangian coordinates, the inverse of $[J]$ must exist, meaning that the jacobian determinant of the jacobian matrix must be nonzero at every point of (ξ,η) in the domain. An eight-node (second-order) quadrilateral element is more complex and, according to the Abaqus 6.10 Theory Manual 3.2.4, its interpolation function written as

$$\begin{aligned} z=&-\frac{1}{4}(1-\xi)(1-\eta)(1+\xi+\eta)z_1-\frac{1}{4}(1+\xi)(1-\eta)(1-\xi+\eta)z_2\\ &-\frac{1}{4}(1+\xi)(1+\eta)(1-\xi-\eta)z_3-\frac{1}{4}(1-\xi)(1+\eta)(1+\xi-\eta)z_4\\ &+\frac{1}{2}(1-\xi)(1+\xi)(1-\eta)z_5+\frac{1}{2}(1-\eta)(1+\eta)(1+\xi)z_6\\ &+\frac{1}{2}(1-\xi)(1+\xi)(1+\eta)z_7+\frac{1}{2}(1-\eta)(1+\eta)(1-\xi)z_8 \end{aligned} \tag{6.9}$$

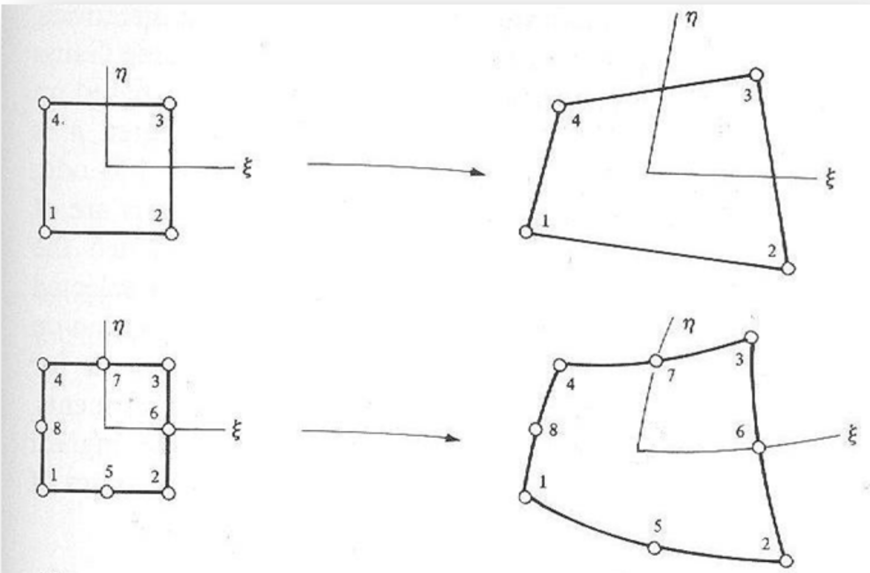

Figure 6-4: First-order and second-order quadrilaterals and their transformations (Reddy, 1984).

As for the displacement model, displacement components u and v in cartesian coordinates are found by using a similar formulation:

$$\begin{Bmatrix} u \\ v \end{Bmatrix} = \begin{bmatrix} \{N_1\}^T \{0\}^T \ldots \{N_8\}^T \{0\}^T \\ \{0\}^T \{N_1\}^T \ldots \{0\}^T \{N_8\}^T \end{bmatrix} \begin{Bmatrix} \{d_1^u\} \\ \{d_1^v\} \\ \ldots \\ \ldots \\ d_8^u \\ d_8^v \end{Bmatrix} = [N]\{d\} = \{u\} \qquad (6.10)$$

where

$\{u\}$ = Displacement vector;

$\{d\}$ = Nodal displacement vector; and

$[N_n]$ = Shape function for node number n.

The strain at each node within an element must be determined, and can be expressed as $\{\varepsilon\}$ having components ε_x, ε_y and γ_{xy}. Strain can be obtained by using a transformation matrix $[B]$ with the displacement vector $\{u\}$ having components u and v.

$$\{\varepsilon\} = [B]\{u\} \qquad (6.11)$$

The transformation matrix $[B]$ contains the derivatives of the interpolation function and $[B] = [B_1, B_2]$ where B_i represents a sub-matrix applied to each node in the element. Once the strain vector $[\varepsilon]$ is determined, the stress vector can be found by using Hooke's law:

$$\{\sigma\} = [C]\{\varepsilon\} \qquad (6.12)$$

Where $[C]$ is the constitutive matrix. Inserting Eq. (6.11)into Eq. (6.12), we have

$$\{\sigma\} = [C][B]\{u\} \qquad (6.13)$$

and finally, the global stiffness matrix $[K]$ can be obtained by manipulating matrices $[C]$ and $[B]$.

$$[K]=\int_V [B]^T [C][B]dV \tag{6.14}$$

Since double integration is quite cumbersome to solve, numerical methods are applied for approximation. For second-order isoparametric elements, Abaqus® solves using Gauss quadrature because of its efficiency (Abaqus 6.10 Theory Manual 3.2.4). The more refined the elements are in the model, the closer the output results will be to the exact solution. However, this increases the number of equations, computational effort and overall simulation time. The nodal displacements in each element must be interpreted or interpolated into cartesian coordinates, for they are written in Lagrangian coordinates.

Written in lagrangian code, Abaqus® provides two isoparametric elements: quadrilaterals for two-dimensional applications and hexahedra (“bricks”) for three-dimensional applications. It is worth noting that the term quadrilateral implies a four-sided element in which its sides are not necessarily of equal length nor have 90 degree corners; in many models sides are curved. Isoparametric elements use symmetric topology mapping, solution approximation function spaces and account for a better domain discretization. Triangular elements are also useful and have their advantages:

1. They consist of complete polynomials;
2. Relatively easy to compute;
3. Less time consuming;
4. Capable of fitting into awkward spots in the mesh.

Nonetheless, isoparametric quadrilateral elements have their own advantage by being more cost-effective of the elements that are provided in Abaqus®, and well-shaped isoparametric elements are better for critical regions in the mesh such as an area where the strain must be predicted accurately (Abaqus 6.10 Theory Manual 3.2.1). They can also degenerate to make simpler shapes for particular geometries. First-order elements are mostly constant strain elements: isoparametric forms

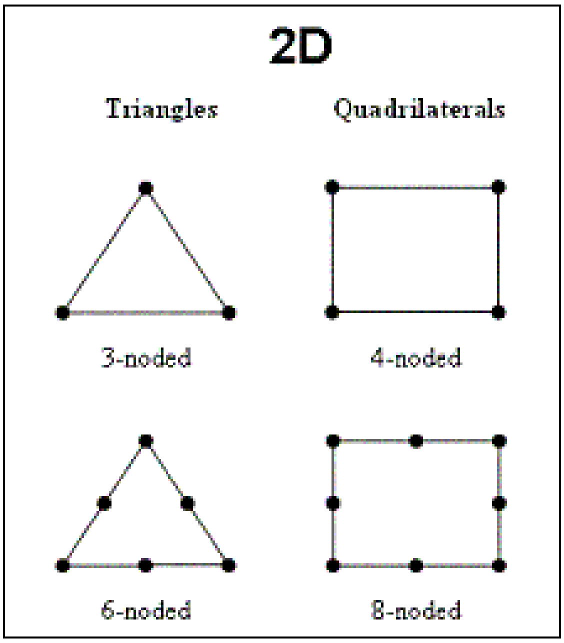

Figure 6-5: 2D elements. (http://stochasticandlagrangian.blogspot.com/2011/07/what-does-shape-function-mean-in-finite.html).

can model this, however second-order elements are capable of representing all possible linear strain fields. Though not the case for this research, another drawback first-order elements have is their poor representation of strain variations in problems involving bending of thin members. This strain variation through the thickness must at least be linear. The use of second-order elements is more reliable since they naturally possess the linear strain field, and one element is sufficient to represent this behavior. Another advantage that second-order equations have is that they are better for elliptic problems including elasticity such as in this research. Also, a much higher accuracy per degree of freedom is usually available with higher-order elements (Abaqus 6.10 Theory Manual 3.2.1). For further reading in regard to the finite element method, please consult the literary resources from Desai et al. (1979, 1984) and Bathe (1982) in the Bibliographic References.

Constitutive models are required for each material. For the reasons stated in Chapters 3 and 4, the casing is chosen to be modeled as elastic perfectly plastic using Hooke's law (see Ch. 2) combined with the von Mises criterion (see Ch. 4.2); the cement as elastic perfectly plastic, applying the Mohr-Coulomb criterion (see Ch. 4); the salt rock as elasto/visco-elastic by using the double mechanism (see Ch. 3.8.4).

Material	Constitutive Models	Formula
Casing (elastic perfectly plastic)	*1. Generalized Hooke's Law*; 2. *von Mises*.	$\varepsilon_i = \frac{1}{E}\left[\sigma_i - \upsilon\left(\sigma_j + \sigma_k\right)\right]$ $\sigma_{vm} = \frac{1}{\sqrt{2}}\sqrt{\left(\sigma_1 - \sigma_2\right)^2 + \left(\sigma_2 - \sigma_3\right)^2 + \left(\sigma_1 - \sigma_3\right)^2}$
Cement (elastic perfectly plastic)	*1. Generalized Hooke's Law*; 2. *Mohr-Coulomb*.	$\varepsilon_i = \frac{1}{E}\left[\sigma_i - \upsilon\left(\sigma_j + \sigma_k\right)\right]$ $\boldsymbol{\tau} = \boldsymbol{c} + \boldsymbol{\sigma}\tan\boldsymbol{\varphi}$
Tachyhydrite (elasto/visco-elastic)	*Double mechanism*.	$\dot{\varepsilon} = \dot{\varepsilon}_0 \cdot \left(\frac{\sigma_{dev}}{\sigma_0}\right)^n \cdot e^{\left(\frac{Q}{RT_0} - \frac{Q}{RT}\right)}$

Table 6-1: Constitutive models used for the three distinct materials.

6.3
Plane Strain Theory

Since three-dimensional modeling is relatively complex and computationally time consuming, a simplified two-dimensional analysis was appropriate and made possible in virtue of the *plane strain theory*. The plane strain theory is a 2D analysis of a slice of a continuous body that assumes that all the points remain on this plane. It is used when the body's longitudinal length is great compared to its width, making it sensible to assume a strain equal to zero in this axis. In other words, the deformations outside the plane are assumed to be zero (Pagano et al., 1967). There are a total of eight variables that are determinable in plane strain, namely σ_x, σ_y, τ_{xy}, ε_x, ε_y, γ_{xy}, u and v. In this research, the well depth represents the longitudinal length.

6.4
Modeling Assumptions

Prior to beginning model simulation, an outline of the assumptions was established:

- ✓ The model considers the state of the wellbore as plane strain.
- ✓ There is a specific state of stress in the salt rock before drilling.
- ✓ The tachyhydrite layer is isotropic, homogeneous and non-porous. The casing and cement are also considered isotropic except for the poorly-cemented regions in the annulus.
- ✓ The cement defect covers a single area and hence not scattered throughout the annulus.
- ✓ The cement is perfectly bonded to the casing and formation, having no gaps along the interfaces.
- ✓ Cement cracking is not accounted for.
- ✓ The in situ stresses are three dimensional and independent of time.
- ✓ The wellbore is vertical.
- ✓ Internal pressure inside the casing (i.e., drilling fluid) is accounted for.
- ✓ The salt formation is impermeable.
- ✓ Thermal properties of the cement, casing and tachyhydrite are negligible.
- ✓ Although well symmetry could be utilized, the model size was not reduced since the defected areas are subject to change during the analysis phase.
- ✓ Casing ovalization of 1.5 percent is induced by compression from the overburden pressure.

6.5 Analytical Solution

6.5.1 Elastic Stresses Around a Wellbore

Before implementing well simulations, an analytical solution must be used to verify that the model is accurate and reliable. Different material properties are used in the analysis; hence each material will be assigned an analytical solution. For elastic, homogeneous, isotropic, continuous and linearly elastic materials, the Kirsch solution may be employed. This exact solution is suitable for the steel casing and cement when loaded within their elastic regions. The Kirsch solution is a 2D plane strain approximation (Goodman, 1989) and consists of the subsequent equations:

$$\sigma_r = \frac{p_1+p_2}{2}\left(1-\frac{a^2}{r^2}\right)+\frac{p_1-p_2}{2}\left(1-\frac{4a^2}{r^2}+\frac{3a^4}{r^4}\right)\cos 2\theta \qquad (6.15)$$

$$\sigma_\theta = \frac{p_1+p_2}{2}\left(1+\frac{a^2}{r^2}\right)-\frac{p_1-p_2}{2}\left(1+\frac{3a^4}{r^4}\right)\cos 2\theta \qquad (6.16)$$

$$\tau_{r\theta} = -\frac{p_1-p_2}{2}\left(1+\frac{2a^2}{r^2}-\frac{3a^4}{r^4}\right)\sin 2\theta \qquad (6.17)$$

Where

$\sigma_r =$ Radial stress, or stress in the direction of changing r;

$\sigma_\theta =$ Tangential stress, or stress in the direction of changing θ;

$\tau_{r\theta} =$ Shear stress; and

$\theta =$ Angle measured counterclockwise from the x axis on the xy plane.

Given a point in a medium using polar coordinates *r, θ* near the hole having radius *a*, the stresses σ_r, σ_θ and $\tau_{r\theta}$ can be determined.

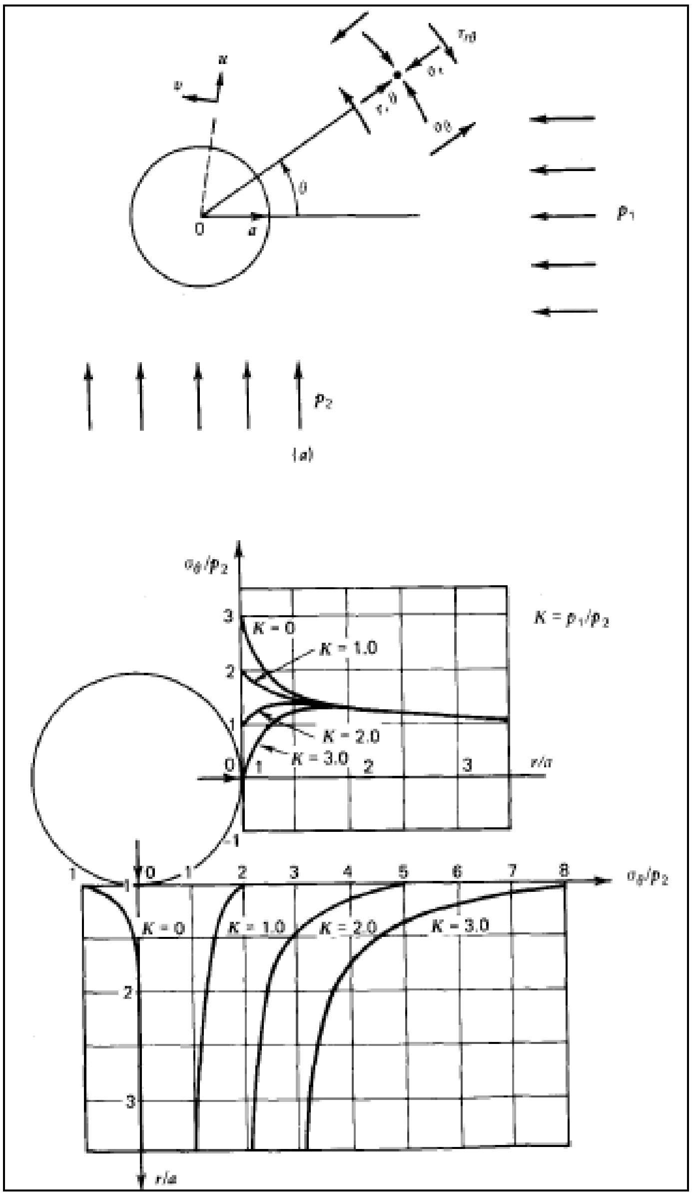

Figure 6-6: Kirsch solution identifies stresses in a medium (Goodman, 1989).

A simple hole-in-a-plate model was used in Abaqus® in order to verify the output data of the program. The model was composed of a total of 2,000 eight-node quadrilateral elements for plane strain continuum (element type *CPE8* in Abaqus®). By taking advantage of the square plate's symmetry, only ¼ of the model was simulated, constraining the left and lower boundaries. The left boundary impeded horizontal displacement while the lower boundary impeded vertical displacement. A single steel-like material was assigned to the model with properties given in Table 6-2 and results in Figure 6-8 and Figure 6-9.

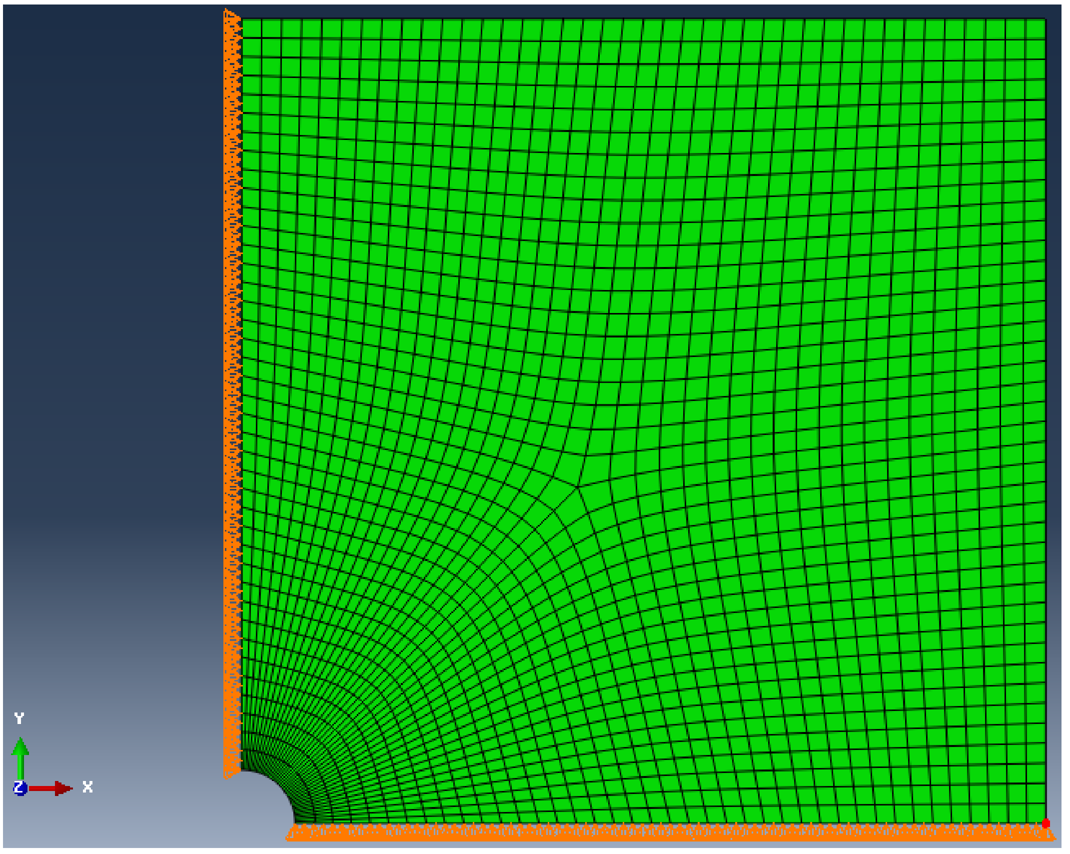

Figure 6-7: Kirsch hole-in-a-plate model in Abaqus.

Stress & Material Properties	Values	Geometry	Values
Young's modulus (*E*)	3.0E+06 MPa	**Height**	15 m
Poisson's ratio (ν)	0.3	**Width**	15 m
Horizontal to vertical pressure ratio ($K=p_1/p_2$)	1, 2, 3	**Hole radius**	1 m

Table 6-2: Model data for Kirsch solution.

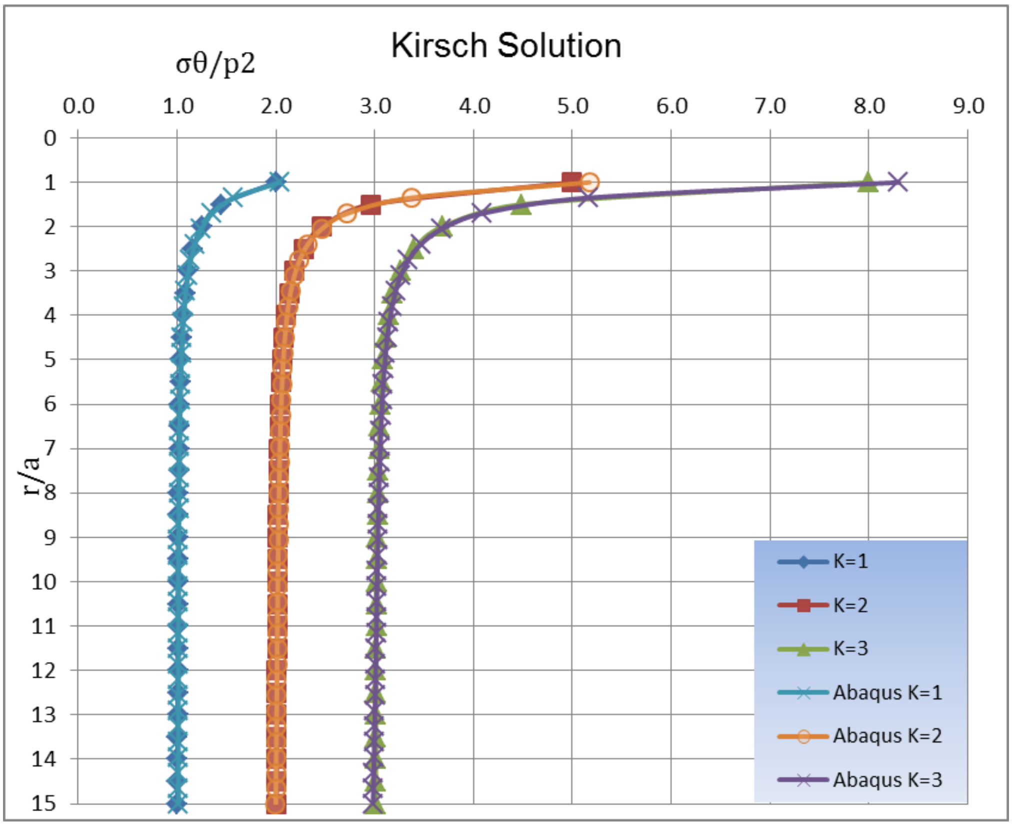

Figure 6-8: Abaqus results using the Kirsch solution (θ=270°) which correspond to the graph shown in Figure 6-6.

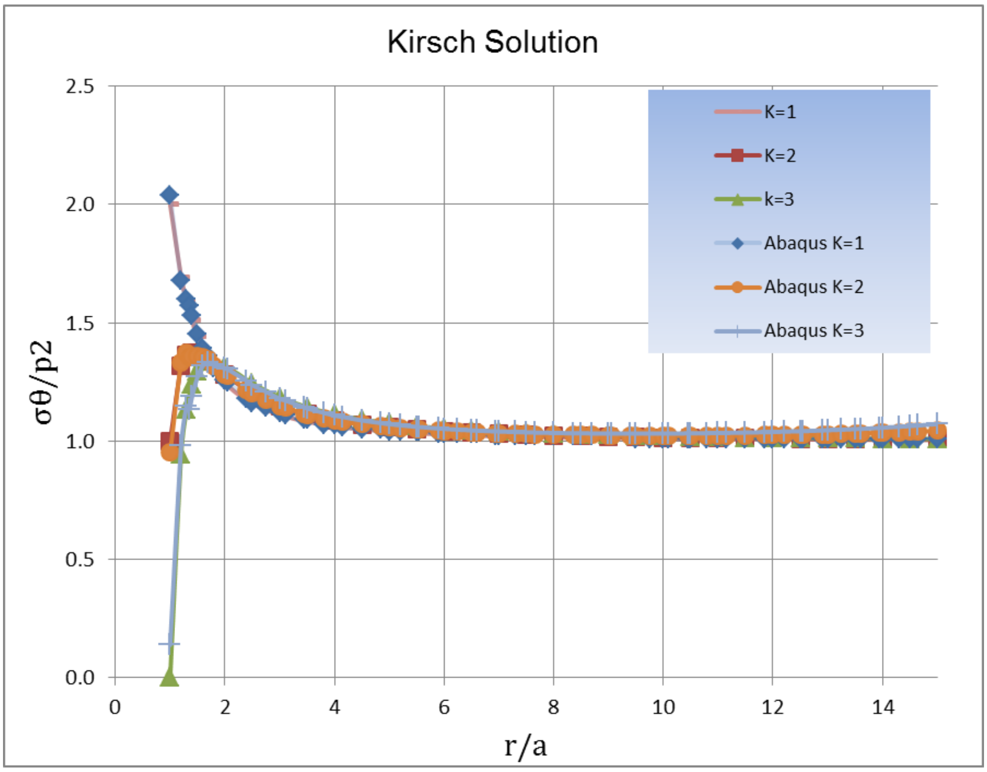

Figure 6-9: Abaqus results using the Kirsch solution (θ=0°) which correspond to the graph shown in Figure 6-6.

Finally, the Abaqus® model was verified to have stress convergence as the distance from the circular hole increases (see Figure 6-10).

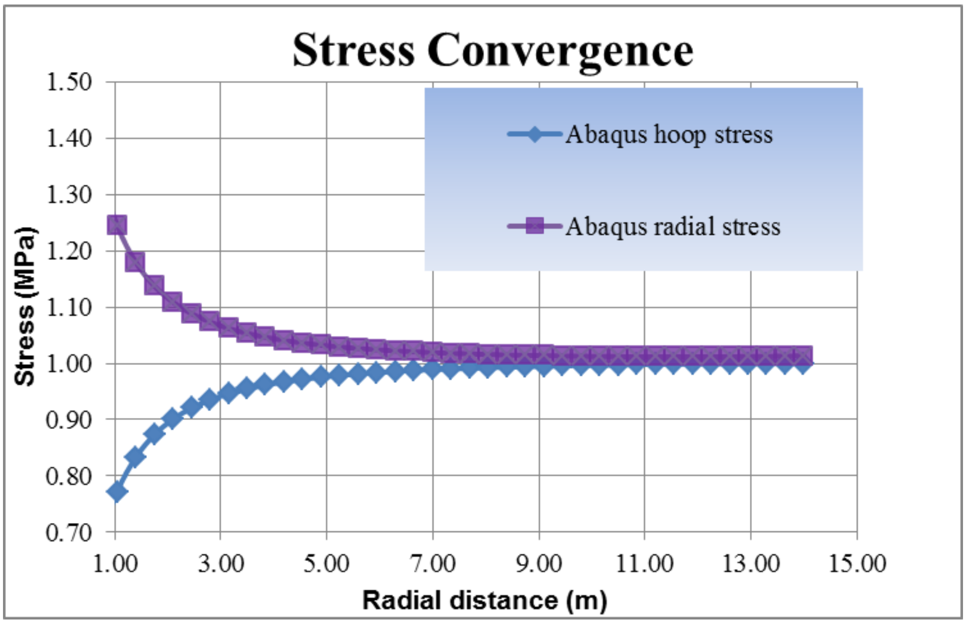

Figure 6-10: Abaqus model results for radial and hoop stress convergence.

6.5.2 Viscoelastic Model

An exact solution for a viscoelastic model is necessary in regard to the salt formation. Thus the van Sambeek model was adopted as the salt rock's analytical solution. This viscoelastic solution is applicable for a power-law creep model of an infinitely long, thick-walled cylinder subjected to pressure on its outer surface. Despite that the double mechanism creep model is being used in this research, it is still valid for comparison with the single-component power law:

$$\dot{\varepsilon} = A\bar{\sigma}^n \quad (6.18)$$

The aforementioned symbols can be reviewed in Chapter 3.7. Knowing the parameters in Eq. (6.18), the van Sambeek steady-state solution (Flac^{3D} v4.0, 1.5.3) can be used and is expressed as

$$\sigma_r = -P_b + P_b \left[\frac{\left(b/r \right)^{2/n} - 1}{\left(b/a \right)^{2/n} - 1} \right] \tag{6.19}$$

$$\sigma_\theta = -P_b - P_b \left[\frac{\left[(2-n)/n \right] \left(b/r \right)^{2/n} + 1}{\left(b/a \right)^{2/n} - 1} \right] \tag{6.20}$$

$$\sigma_z = -P_b - P_b \left[\frac{\left[(1-n)/n \right] \left(b/r \right)^{2/n} + 1}{\left(b/a \right)^{2/n} - 1} \right] \tag{6.21}$$

$$\dot{u}_r = -A \left(3/4 \right)^{(n+1)/2} \left[P_b \frac{2/n}{\left(b/a \right)^{2/n} - 1} \right]^n \left(b^2/r \right) \tag{6.22}$$

Where

σ_z = out-of-plane stress component;

P_b = applied boundary stress;

$\dot{u}_r$ = radial displacement rate;

r = radius to point of calculation; and

a, b = inner and outer radii of the cylinder, respectively.

The same procedure from the Kirsch solution was carried out, using the same mesh, geometry, boundary conditions and element type. The material properties, however, were modified for modeling convenience and are shown in Table 6-3.

Stress & Material Properties	Values
Young's modulus (*E*)	820 MPa
Poisson's ratio (ν)	0.3636
Reciprocal viscosity coefficient (*A*)	5.3E-14 MPa^{-3} h^{-1}
Stress power (*n*)	7.55
Pressure (P_b)	10 MPa

Table 6-3: Model data for van Sambeek solution.

Prior to proceeding with the analysis, it was verified that the model reached the steady-state regime shown in Figure 6-11.

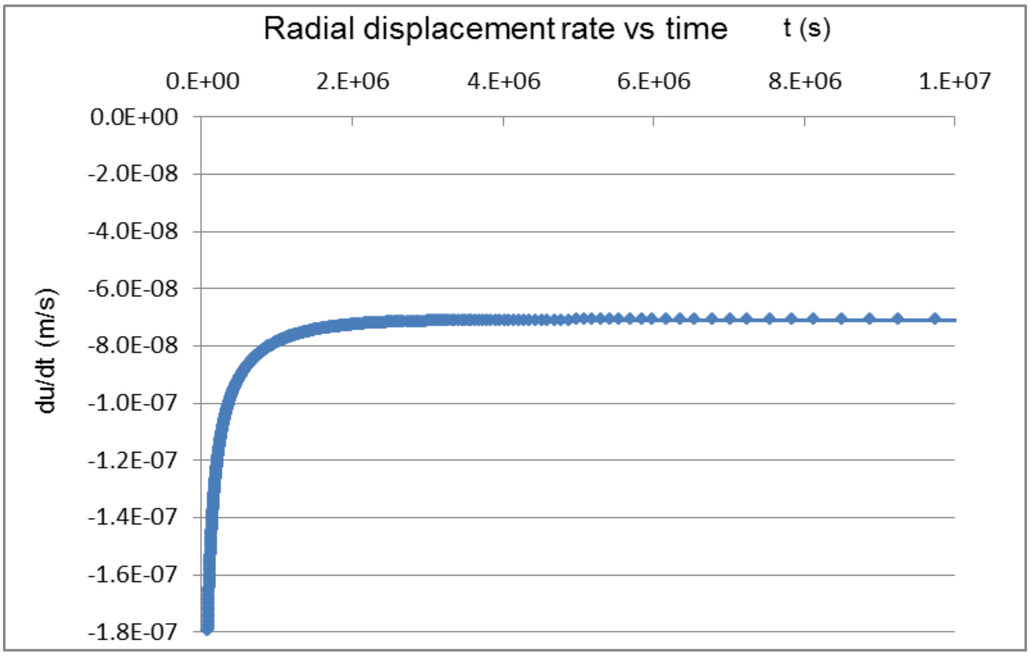

Figure 6-11: The viscoelastic model generated in Abaqus reaches steady state.

The model's viscoelastic behavior at steady-state was compared to the van Sambeek solution, showing good agreement in terms of σ_r, σ_θ and $\dot{u}_r$. Confirming both the accuracy of the Kirsch solution and van Sambeek solution along with Abaqus' reliability, it is safe to proceed to the modeling sequences.

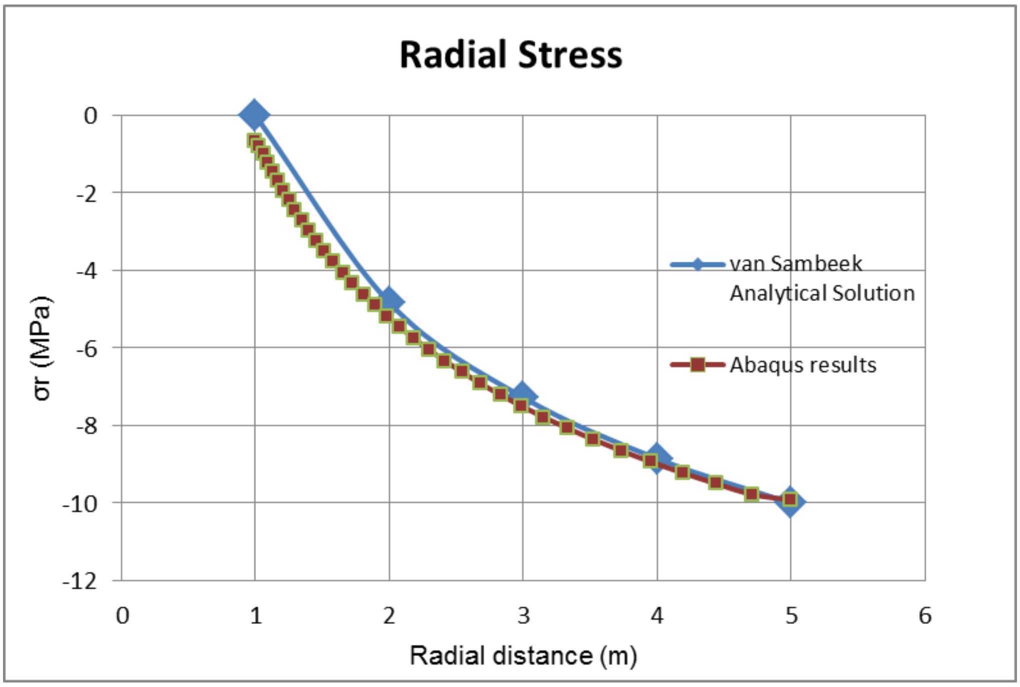

Figure 6-12: Radial stress results at steady-state condition.

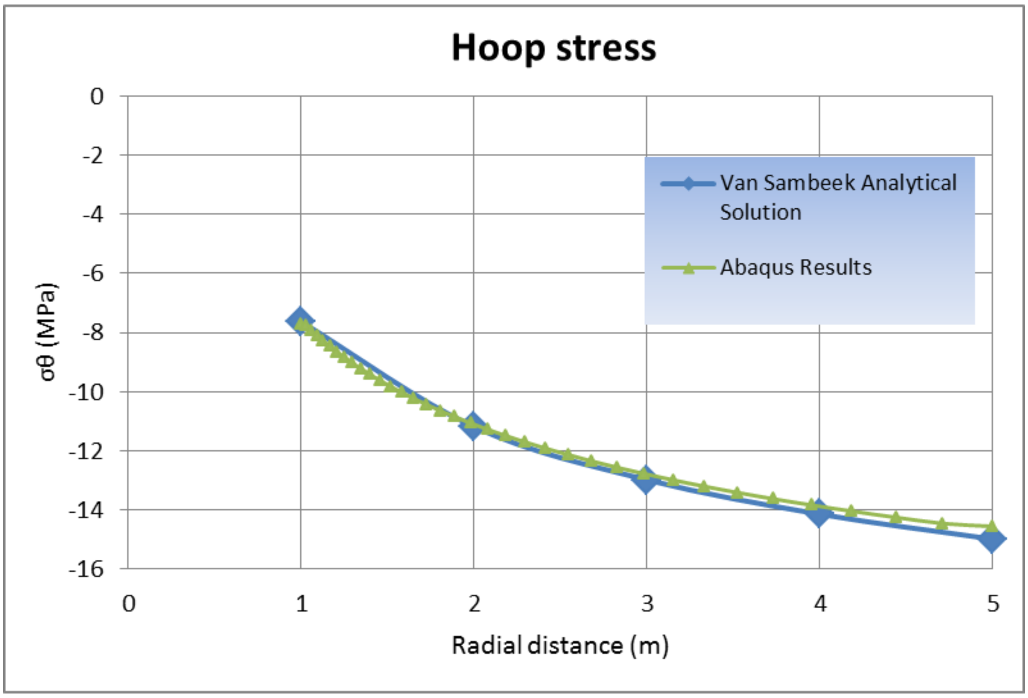

Figure 6-13: Hoop stress results at steady-state condition.

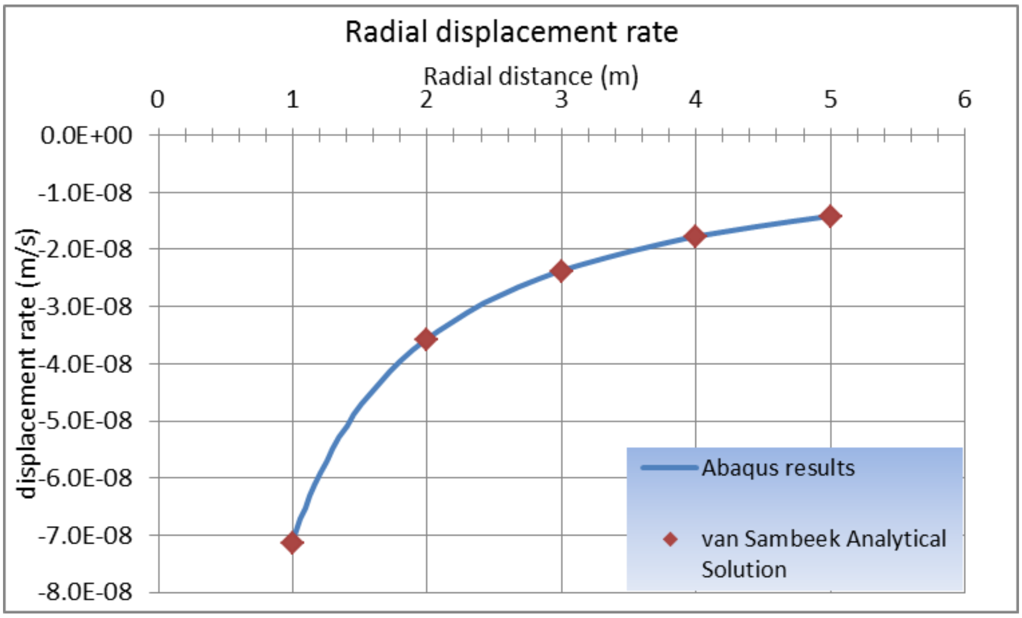

Figure 6-14: Radial displacement rate results.

6.6 Model Description

The two-dimensional plane strain model used in the analysis was designed to be perpendicular to the vertical axis of the wellbore—similar to a plan view layout—and consisted of the three distinct materials: the steel casing, cement and salt rock. The model was created with a circular outer boundary of 100 m in diameter having a 0.445 m diameter wellbore and composed of 20,442 quadratic isoparametric elements with a total of 46,326 nodes. In this model, each element consists of eight nodes and all were assigned the Abaqus element type CPE8: eight-node continuum stress/displacement plane strain element. This element type was selected as opposed to four-node and three-node elements for the sake of requiring fewer elements and also to increase accuracy in critical regions that appear in the narrow annulus due to high eccentricity. A subroutine was used in Abaqus® in order to implement the double mechanism constitutive salt creep law proposed by Costa (2005) and Poiate et al. (2006) for tachyhydrite. After conducting laboratory experiments on salt samples collected from Sergipe, Brazil, Poiate et al. (2006) observed a sudden shift for both tachyhydrite's and halite's mechanical behavior. The strain rate for each sample was obtained by applying a differential stress ranging from 0 to 20 MPa at a temperature of 86ºC. During the steady state creep stage, the stress component *n* for tachyhydrite changes from 2.4 to 7.12 after a 7 MPa differential stress. Recalling Eq. (3.14) from Chapter 3.8.4, the double mechanism formula consists of two stresses, namely the deviatoric stress σ_{dev} and the referential stress σ_0, where the former represents the differential stress varying with time while the latter is the stress value (e.g., 7 MPa) at which shifting occurs. This subroutine was verified with the results from Poiate et al. (2006) shown in . With the Abaqus result superimposed in this figure, it should be noted that Poiate’s graph shows the time of drilling beginning at a depth of zero. Thus, the time of drilling the tachyhydrite layer begins at approximately 192 hrs. The results show good agreement, proving the proposed subroutine to be acceptable. It is also important to note the horizontal deviation of the Abaqus curve being the result of the introduction of the casing and cement.

Tachyhydrite

$$\dot{\varepsilon} = \dot{\varepsilon}_0 \left(\frac{\sigma_{ef}}{\sigma_0}\right)^n \exp\left(\frac{Q}{RT_0} - \frac{Q}{RT}\right)$$

ε_0 = 1.1E-04 h^{-1}

σ_0 = 7MPa

T_0 = 86ºC = 359K

Q = 12 kcal/mol,

R = 1.9858E-03 kcal/mol.K

n = 2.40, $\sigma_{ef} < \sigma_0$

n = 7.12, $\sigma_{ef} < \sigma_0$

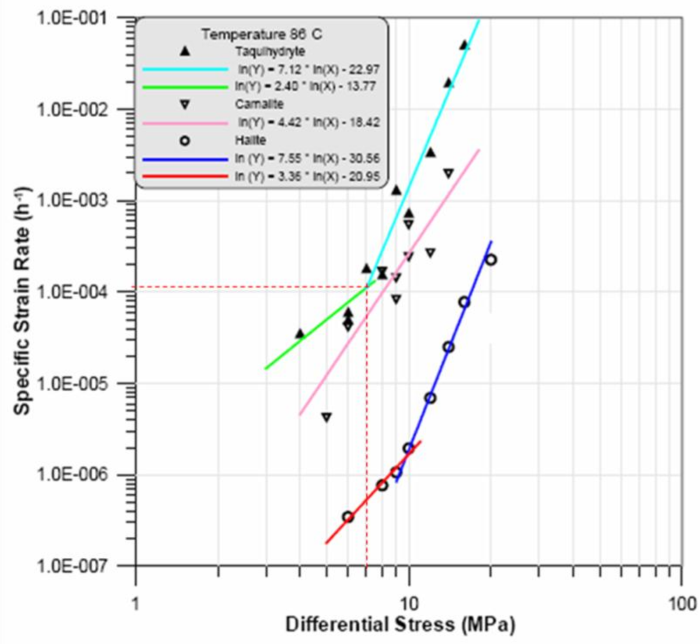

Figure 6-15: Data (left) used in the double mechanism equation to approximate the tachyhydrite behavior shown in the graph (right) provided by Poite et al. (2006).

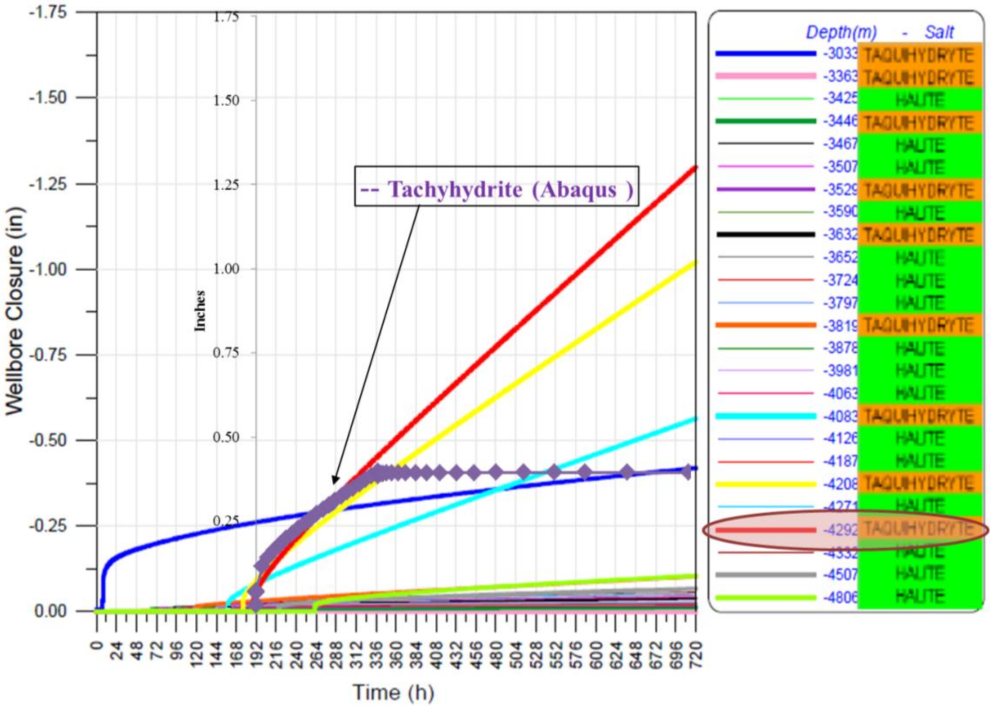

Figure 6-16: Abaqus tachyhydrite subroutine result (purple) compared with Poiate et al. (2006) tachyhydrite result (red).

6.7 Boundary Conditions

The idea of imposing boundary conditions can be thought of as imposing a physical support on a model’s extremities, with the purpose of defining or approximating how the material external to the simulation domain influences it. Fixed ends were assigned to the model’s outer boundary as well as for the casing. In other words, displacement was permitted in neither of these. The casing however, is fixed only in the equilibrium stage of the modeling sequence but for the rest of the model was left free to move unbounded. This was done to avoid initial computation errors that may precipitate throughout the simulation. A detailed explanation of the modeling sequence is discussed later in this chapter. Initial stresses were assigned to the model’s exterior boundary as well as an out-of-plane stress to simulate the overburden stress.

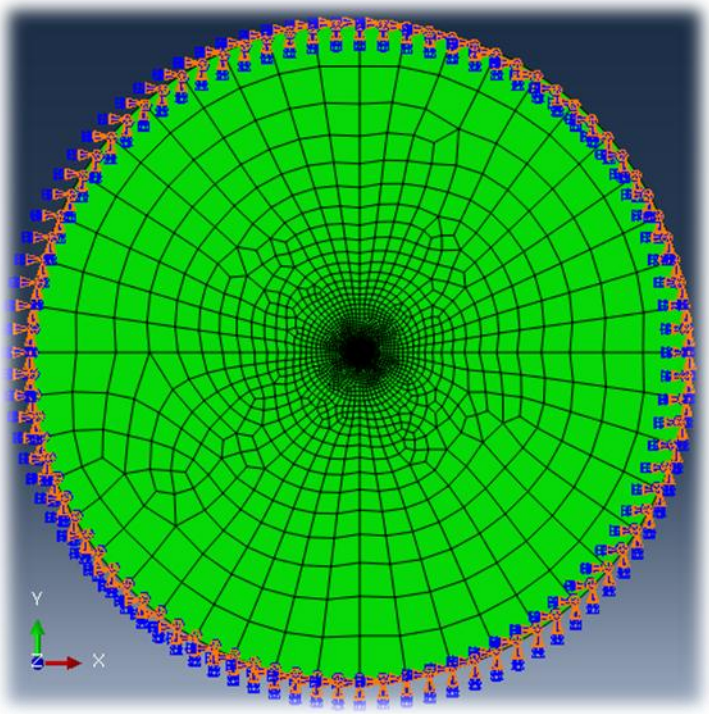

Figure 6-17: Imposed fixed boundary conditions on the model’s exterior surface.

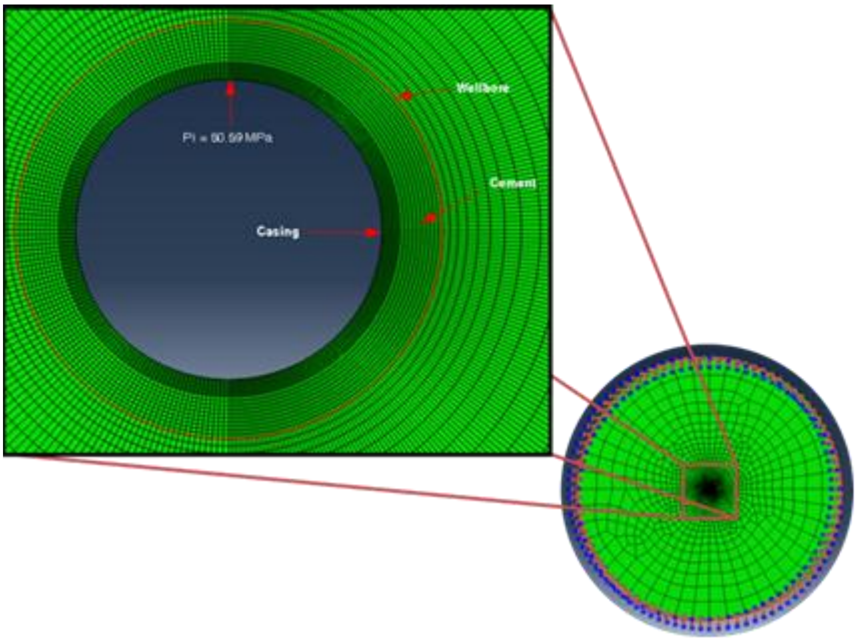

Figure 6-18: Model zoom showing elements for the casing and cement.

Since salt rock is isotropic, the horizontal and vertical loads induced upon the cemented casing are equal to a magnitude of 70.2 MPa and remains constant throughout the analysis. For verification purposes, the drilling fluid pressure within the casing was compared with values of 65.87 MPa (~13 ppg) and 50.59 MPa (~9.98 ppg).The results indicate that the internal pressure of 50.59 MPa is more appropriate for simulation purposes as opposed to 65.87 MPa since a greater pressure differential relative to the salt creep provokes a higher compressive stress, creating a more critical and interesting scenario that offers a better understanding of the effects of salt creep.

6.8
Model Data

Material properties for the steel casing, cement and salt rock were assigned to their corresponding sections in the model. All material properties used in the modeling were gathered from available literature: Poiate et al. (2006) and Bosma (1999). Competent cement was selected for the analysis since high compressive strength slurries are used for deep wells (Fleckenstein, 2000). A steel grade of P-110 (yield strength of 110,000 psi or 758 MPa) and an OD of 14 inches are suitable property and geometric characteristics for a 4301 m depth.

Material properties	Young's Modulus, E (MPa)	Poisson's ratio, ν
Salt Rock (tachyhydrite)	4,920	0.33
Cement (Class G)	21,000	0.25
Casing (14" X 0.722" - P110)	210,000	0.28

Table 6-4: Elastic properties for the salt rock, cement and steel casing.

Material	Thickness (m)	Specific weight (kN/m^3)	Vertical Stress σ_z (MPa)
Seawater	2140	10	21.40
Salt layer	1303	22.56	29.69
Other layers	858	22.56	19.36
Total σ_z at studied depth 4301 m			70.20

Table 6-5: Vertical stress induced upon the cemented casing.

Reviewing his work, Poiate et al. (2006) used an ovalization value of 1.5 percent— Eq. (5.2) was verified by superimposing the oval geometry over the circular 14-inch P-110 casing. This ovality was compared with Pattillo's formula given in Eq. (5.1) which would yield a value of 3.0 percent, a value nearly ten times that of an initial manufacturing ovality as seen in Pattillo et al. (2004) and Aldin et al. (1998). Hence, an ovality of 1.5 percent in terms of Poiate's formula would be significant enough to affect the cement's stress state and condition.

Initial wellbore diameter	17 ½ inches (0.4445 m).
Casing dimensions	14" x 0.722" (OD = 0.3556 m, E = 0.0183 m).
Ovalization (1.5%)	OD_{max} = 0.3609 m, OD_{min} = 0.3503 m.

Table 6-6: Wellbore and casing data.

For employing the power creep law, Abaqus® gives two options: The time hardening form and the strain hardening form. The time hardening formulation can be expressed as

$$\varepsilon = A\sigma^n t^m \tag{6.23}$$

and by taking its derivative with respect to time *t*, it can be written as

$$\dot{\varepsilon} = A\sigma^n m t^{m-1} \tag{6.24}$$

By solving for t in Eq. (6.24) and substituting it back into the formula, the strain hardening formulation is obtained:

$$\dot{\varepsilon} = A^{1/m} m \sigma^{n/m} \left(\varepsilon\right)^{m-1/m} \tag{6.25}$$

Of these two formulations, the time hardening form was selected for the model because it is ideal for simulating deformations over long periods of time in which the stress state does not vary rapidly (Botelho, 2008), whereas the strain hardening formulation is more appropriate for a rapidly changing stress state. Furthermore, it is the simplest form of the power law and Botelho's work demonstrates its accuracy and reliability in Abaqus® for salt wellbore drilling simulations.

6.9 Modeling Sequence

The intention of the model is to simulate strictly the wellbore drilling phase followed by the casing and cementing phase. The production phase is not considered and is beyond the scope of this work. Though the state of stress of the cement and casing is observed during the period of 28 days, the primary concern is at the end of this period in which the cement attains adequate strength. Instead of simulating three steps, the model was subdivided into five steps.

Step 1: Equilibrium

This step simulates the natural state of stress of the salt formation which has to remain in equilibrium. In other words, it represents the salt zone before drilling. This was simulated by beginning the 2D model—having only the salt rock present—imposing an equal and opposite uniform stress along the face of the initial wellbore diameter as demonstrated in Figure 6-19. This is same as having a continuous salt rock under static equilibrium, and was simulated for one second.

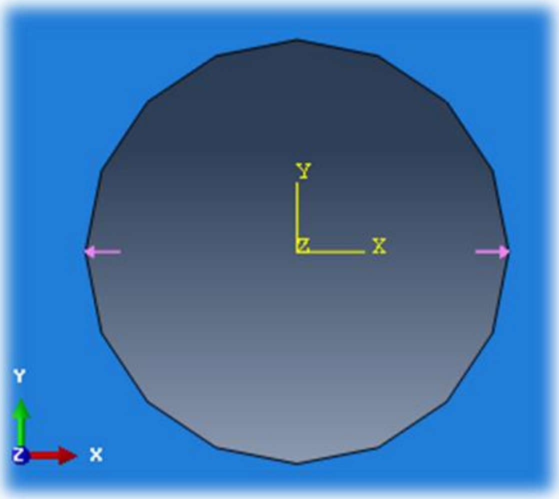

Figure 6-19: Step 1 - Borehole in static equilibrium.

Step 2: Drilling

The drilling step is simulated by removing a circular area from the salt formation. This step was simulated by reducing the balanced uniform stress along the wellbore face to a lower value of 50.59 MPa. This step is simulated for a time of 60 seconds.

Step 3: Drilling continuation

This step is a continuation of the previous step elongating the time. Wellbore closure is simulated for 100 hours (4.17 days).

Step 4: Casing installation and cementing.

The casing and the cement are instantaneously introduced while the salt formation continues to close. The model simulates the cement-salt formation interface to be in complete contact since the cement molds to fit the deformed wellbore face.

Step 5: Well closure

A continuation of the previous step simulating the casing/cement/salt interaction over a period of 28 days.

The analysis was performed using three main stages:

- *Stage 1:* Begin with analyzing the casing and cement having only elastic behavior.
- *Stage 2:* Analyze the casing and cement with elastic and plastic properties (i.e., elastic perfectly plastic).

- *Stage 3:* Analyze the cement with casing eccentricity.

Various scenarios were created to effectively predict and analyze the behavior of a poorly-cemented casing under salt loading.

6.9.1
Stage 1: Cement as an Elastic Material

This initial stage is a simulation that assigns strictly an elastic response for the cement and casing while the salt formation obeys the double mechanism constitutive model. Such an approach prohibits the casing and cement from attaining failure, allowing the stress, strain and displacement values to be observed. In this step, the following scenarios were tested:

Case 1: The geometry of the casing, cement and wellbore are given the shape of a perfect circle.

- Case 1.1: Well-cemented (homogeneous cement with no defects).
- Case 1.2: Ten percent of annulus poorly-cemented (i.e., 10 percent of the cement area having a young's modulus 10 percent, 20 percent and 75 percent weaker than the rest).
- Case 1.3: Twenty percent of annulus poorly-cemented (i.e., 20 percent of the cement area having a Young's modulus 10 percent, 20 percent and 75 percent weaker than the rest).

Case 2: Casing with 1.5 percent ovality.

- Case 2.1: Well-cemented (homogeneous cement with no defects).
- Case 2.2: Ten percent poorly-cemented (i.e., 10 percent of the cement area having a young's modulus 10 percent, 20 percent and 75 percent weaker than the rest).
- Case 2.3: Twenty percent poorly-cemented (i.e., 20 percent of the cement area having a young's modulus 10 percent, 20 percent and 75 percent weaker than the rest).

Table 6-7: Scenarios in Stage 1: Cement as an Elastic Material

The scenarios were analyzed having a poorly-cemented region with an area no greater than 20 percent of the annulus. A hypothesis was made suggesting that a larger area would unlikely be encountered in the field. Moreover, no relevant articles were found suggesting area sizes.

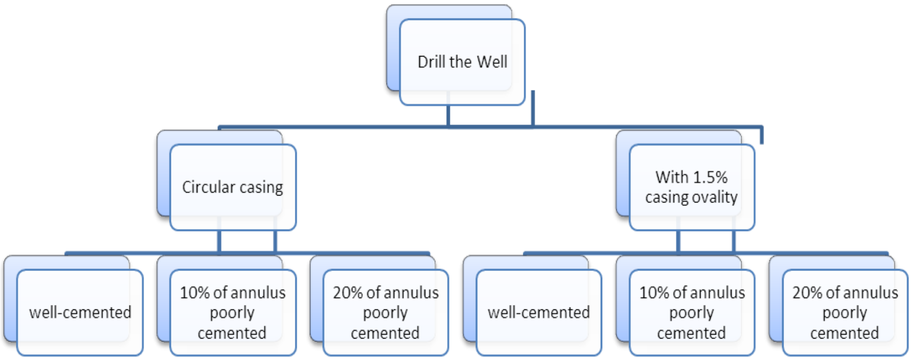

Figure 6-20: Outline of the six simulated scenarios.

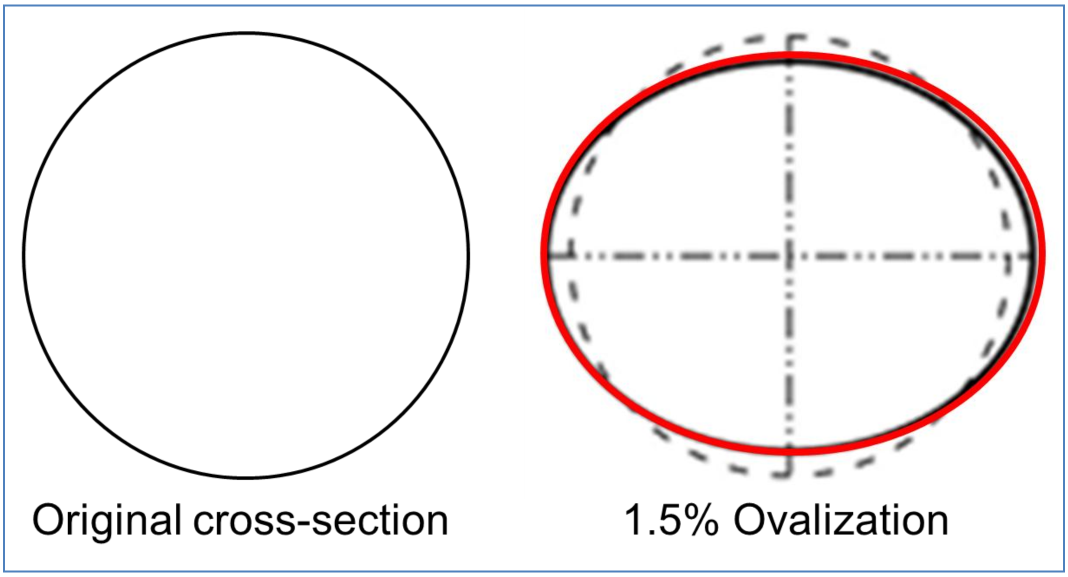

Figure 6-21: Casing ovalization modeled as 1.5%. (Wadee MK et al., 2006). Note: Image not to scale.

6.9.2
Stage 1 Results

The results for the six scenarios were compared in terms of stress, strain and displacement. The preliminary results indicate that a 10 percent or 20 percent reduction in parameters E and v do not have a significant effect on the state of stress. The stresses taken into consideration were the maximum principal stresses, since the stress state at a point is characterized by the principal stresses. The defected cement models with areas of 10 percent and 20 percent show a difference in stress values no greater than 1 percent with respect to the well-cemented model.

The maximum values for strain and displacement are 0.03 percent and 0.0209 m, respectively. The values for strain and displacement in the casing are smaller than those for the cement.

The models with casing ovality of 1.5 percent also exhibit practically the same stress values as the well-cemented model. The same is witnessed for the casing. The strains and displacements are relatively small and also similar to the models having a circular casing. A change is only seen, however, once the poorly-cemented area was modeled with a 75 percent reduction in the elastic parameters. This caused an increase in the stress values in the cement, seeing differences as great as 9 percent with respect to the maximum values for principal stresses.

Observing Table 6-8 through Table 6-13, the elastic model indicates that the tangential stress is dominant for both the casing and cement.

The von Mises stress in the casing never exceeds the SMYS value (758 MPa), meaning that the steel casing is being loaded within the elastic region. This was also verified by observing the differences between σ_1 , σ_2 and σ_3. The induced stresses upon the casing do not provoke significant ovalization.

All scenario results show stresses solely in compression. It should be noted that Abaqus' maximum and minimum values are in reverse due to the sign convention, where a negative sign denotes compression.

CEMENT	Well-cemented annulus.				
E (MPa)	21,000	Stress	σ radial max. (MPa)	σ tangential max. (MPa)	Principal σ max.(MPa)
ν	0.25	Mini graph			
ε max.:	0.03%		-69	-82	-82
u max (m):	0.02	Load Type:	comp.	comp.	comp.
CASING		**OD (y axis) min.**	**OD (x axis) max.**	**Ovalization (%)**	
E (MPa)	210,000				
ν	0.28	3.55E-01	3.55E-01	0.02	
σyield (MPa)	758	Stress Mini graph	σ radial max. (MPa)	σ tangential max. (MPa)	Principal σ max. (MPa)
Mises (MPa)	147		-67	-217	-217
ε max.:	0.03%	Load Type:	comp.	comp.	comp.
u max (m):	0.0001				

Table 6-8: Well-cemented annulus.

CEMENT	10% of cement area with a 75% parameter reduction (*E*,*v*).				
E (MPa)	5,250	Stress	σ radial max.	σ tangential	Principal σ
v	0.25	Mini graph	(MPa)	max. (MPa)	max. (MPa)
ε max.:	0.09%		-70	-82	-89
u max (m):	0.02	Load Type:	comp.	comp.	comp.
CASING		**OD (y axis)**	**OD (x axis)**	**Ovalization**	
E (MPa)	210,000	**min.**	**max.**	(%)	
v	0.28	3.55E-01	3.55E-01	0.01	
σyield (MPa)	758	Stress Mini graph	σ radial max. (MPa)	σ tangential max. (MPa)	Principal σ max. (MPa)
Mises (MPa)	158		-72	-229	-229
ε max.:	0.04%	Load Type:	comp.	comp.	comp.
u max (m):	0.0001				

Table 6-9: 10% of cement area with a 75% parameter reduction (*E*,*v*).

CEMENT	20% of cement area with a 75% parameter reduction (*E*,*v*).				
E (MPa)	5,250	Stress	σ radial max.	σ tangential	Principal σ
v	0.25	Mini graph	(MPa)	max. (MPa)	max. (MPa)
ε max.:	0.10%		-69	-82	-87
u max (m):	0.02	Load Type:	comp.	comp.	comp.
CASING		**OD (y axis)**	**OD (x axis)**	**Ovalization**	
E (MPa)	210,000	**min.**	**max.**	(%)	
v	0.28	3.55E-01	3.55E-01	0.01	
σyield (MPa)	758	Stress Mini graph	σ radial max. (MPa)	σ tangential max. (MPa)	Principal σ max. (MPa)
Mises (MPa)	158		-70	-229	-229
ε max.:	0.04%	Load Type:	comp.	comp.	comp.
u max (m):	0.0001				

Table 6-10: 20% of cement area with a 75% parameter reduction (*E*,*v*).

CEMENT	Well-cemented annulus with 1.5% ovality.				
E (MPa)	21,000	Stress	σ radial max.	σ tangential	Principal σ
v	0.25	Mini graph	(MPa)	max. (MPa)	max. (MPa)
ε max.:	0.04%		-69	-84	-84
u max (m):	0.02	Load Type:	comp.	comp.	comp.
CASING		**OD (y axis)**	**OD (x axis)**	**Ovalization**	
E (MPa)	210,000	**min.**	**max.**	(%)	
v	0.28	3.50E-01	3.61E-01	1.53	
σyield (MPa)	758	Stress Mini graph	σ radial max. (MPa)	σ tangential max. (MPa)	Principal σ max. (MPa)
Mises (MPa)	170		-68	-243	-243
ε max.:	0.04%	Load Type:	comp.	comp.	comp.
u max (m):	0.0002				

Table 6-11: Well-cemented annulus with 1.5% ovality.

CEMENT	10% of cement area with a 75% parameter reduction (*E*,*ν*) with 1.5% ovality.				
E (MPa)	5,250	Stress	σ radial max.	σ tangential	Principal σ
ν	0.25	Mini graph	(MPa)	max. (MPa)	max. (MPa)
ε max.:	0.08%		-70	-84	-90
u max (m):	0.02	Load Type:	comp.	comp.	comp.
CASING		**OD (y axis)**	**OD (x axis)**	**Ovalization**	
E (MPa)	210,000	**min.**	**max.**	(%)	
ν	0.28	3.50E-01	3.61E-01	1.53	
σyield (MPa)	758	Stress Mini graph	σ radial max. (MPa)	σ tangential max. (MPa)	Principal σ max. (MPa)
Mises (MPa)	171		-73	-244	-244
ε max.:	0.04%	Load Type:	comp.	comp.	comp.
u max (m):	0.0002				

Table 6-12: 10% of cement area with a 75% parameter reduction (*E*,*ν*) with 1.5% ovality.

CEMENT	20% of cement area with a 75% parameter reduction (*E*,*ν*) with 1.5% ovality.				
E (MPa)	5,250	Stress	σ radial max.	σ tangential	Principal σ
ν	0.25	Mini graph	(MPa)	max. (MPa)	max. (MPa)
ε max.:	0.12%		-70	-83	-85
u max (m):	0.02	Load Type:	comp.	comp.	comp.
CASING		**OD (y axis)**	**OD (x axis)**	**Ovalization**	
E (MPa)	210,000	**min.**	**max.**	(%)	
ν	0.28	3.50E-01	3.61E-01	1.53	
σyield (MPa)	758	Stress Mini graph	σ radial max. (MPa)	σ tangential max. (MPa)	Principal σ max. (MPa)
Mises (MPa)	179		-70	-253	-253
ε max.:	0.04%	Load Type:	comp.	comp.	comp.
u max (m):	0.0002				

Table 6-13: 20% of cement area with a 75% parameter reduction (*E*,*ν*) with 1.5% ovality.

6.9.3
Stage 2: Cement as an Elastic Perfectly Plastic Material

In this stage, the cement's mechanical properties are changed to *elastic perfectly plastic* while the casing and the salt rock remain unchanged. This is done by adding the Mohr-Coulomb failure criterion in Abaqus®. As mentioned in chapter 4, this failure criterion requires material strength parameters ϕ and c which are empirically determined. In his work, Bosma (1999) obtained reliable results using a Class G cement cohesion value of 21 MPa with an angle of friction of 17 degrees (assuming for 28-day strength). These values were adopted for the analysis.

Once experimental data was received from the rock mechanics laboratory at Petrobras Research Laboratories (CENPES), a comparison was made with Bosma's strength parameters. This was done for the purpose of determining the appropriate values that yield a greater change in the wellbore's state of stress. The experimental results yielded an angle of internal friction of 15.5 degrees and a cohesive strength of 14.5 MPa. The dilation angle is a required input value in Abaqus®, but since it was not given, the parameter was determined by implementing an equation given by M.P Nielson (2010):

$$\sin\varphi = \tan\psi \tag{6.26}$$

where φ is the angle of internal friction and ψ is the dilation angle. This formula yielded a value of 15 degrees. The former set of cement strength parameters was given conservative values to allow for contrast in the scenarios results. It should be noted that the experimental results correspond to 7 days of curing. By manipulating the strength gain graph in Figure 5-10, a 28-day estimate was made possible for the parameters provided by CENPES by extrapolation. The parameters surprisingly yielded nearly the same values as provided by Bosma (1999).

Bosma's Cement Strength Parameters (28 days):	**CENPES Experimental Parameters (7 days of curing):**	**CENPES Estimated Parameters (28 days):**
ϕ = 17.0°	ϕ = 15.5°	ϕ = 15.5°[1]
Ψ = 16.0°	Ψ = 15°	Ψ = 15°
c = 21 MPa	c = 14.5 MPa	c = 21 MPa

Table 6-14: Mohr-Coulomb strength parameters.

Therefore, since these two data results given in
Table 6-14 are almost identical, the strength parameters from Bosma were assigned to the subsequent simulations.

[1] It should be noted that the angle of friction typically remains constant for strength gain.

6.9.3.1
Geometry of the Poorly-Cemented Region

To establish a sensitivity analysis for the mechanism of the defected cement region, it was decided to simulate using three different geometries as shown in Figure 6-22, and in this research they will be referred to as Geometry No. 1, Geometry No. 2 and Geometry No. 3, respectively.

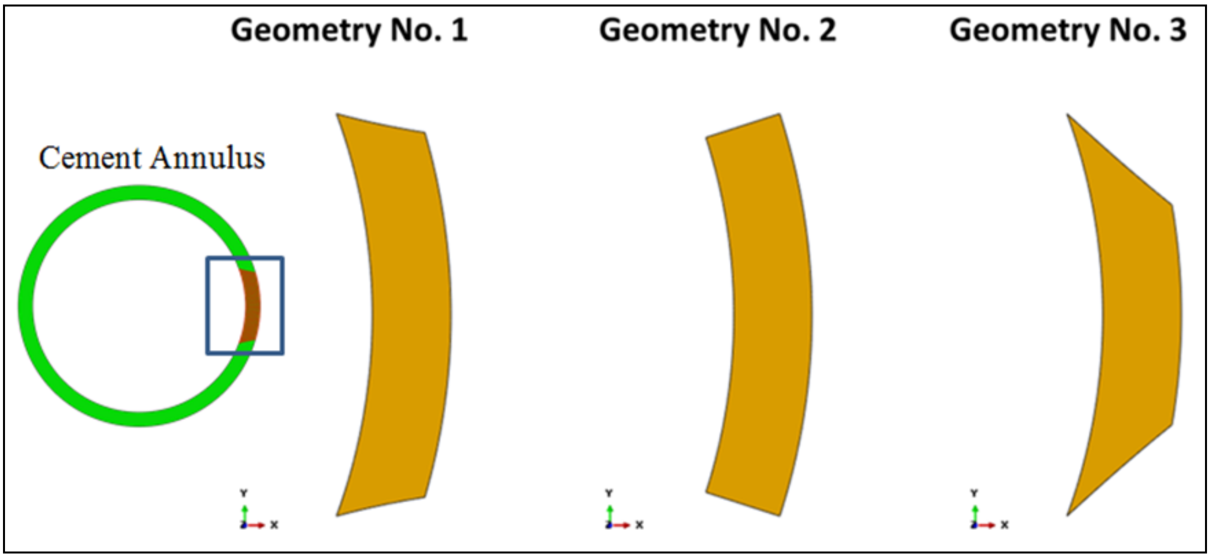

Figure 6-22: Three different geometries for the damaged cement region.

The following objectives were defined for Stage 2:

- Identify what percent reduction of the cement parameters *E*, *v* and *c* in the defected region provokes plasticity.
- Simulate using a substantially higher percent reduction and compare results with the previous percent reduction.
- Analyze further by comparing the stress states for the geometries for areas of 5 percent, 10 percent and 20 percent of the annulus.
- Identify what type of stress is most critical for the defected cement region and its location.
- Interpret from the stress magnitude and its location what is occurring.
- Observe the effect, if any, that casing ovalization has upon the cement.

6.9.4
Stage 2 Results

The simulation results shown in Figure 6-23 indicate that plasticity appears in the defected cement region in all the geometries and areas (i.e., 5%, 10% and 20%) when parameters *E*, *v* and *c* reduce to only 15 percent. This plastic straining is controlled by the compressive stress induced by the surrounding tachyhydrite layer. The poorly-cemented region fails due to high dilation which stabilizes the scenario. The stress state in this case, however, does not show any significant increase when compared to the well-cemented model. After several simulation tests, it was found that the stress levels for the cement and casing became significant at a 75 percent stiffness and cohesion reduction.

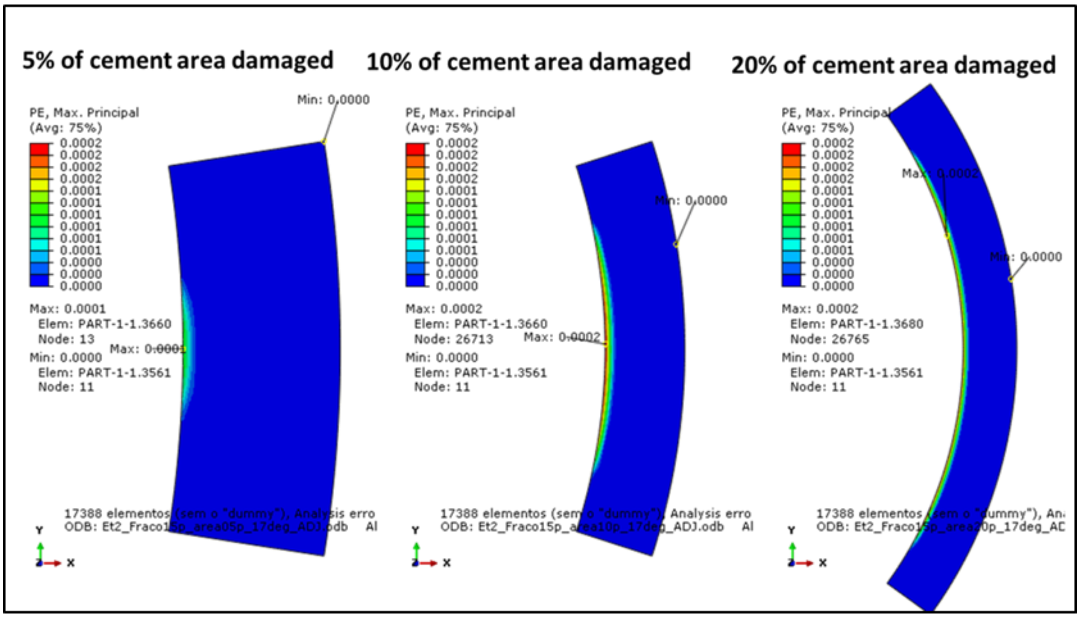

Figure 6-23: Plasticity results for Geometry No. 1; when parameters *E*, *v* and *c* reduce to only 15 percent.

Observing the Mises stress, there were no occurrences where the steel casing reached its SMYS limit of 758 MPa in any of the analyses. Moreover, the casing shows values of displacement and strain at approximately 0.028 cm and 0.045 percent, respectively. These results suggest to model the casing merely as elastic. With a 75 percent reduction in the parameters *E*, *v*, and *c*, the maximum stress values in the cement become significantly greater by at least 82 percent compared to the results with a 15 percent reduction. These values are located on the upper and lower boundaries of the poorly-cemented region. The greatest maximum principal stress is found in Geometry No. 3 with an increase of almost 130 percent compared to the well-cemented model.

Unexpectedly, the results such as in Figure 6-24 indicate that a 10 percent area is where the maximum stress appears for all geometries and areas. The maximum stresses, however, are always found along the upper and lower boundaries of the defected cement area. These border lines show an angle closer to forty-five degrees at a 10 percent area than do the areas of 5 percent or 20 percent.

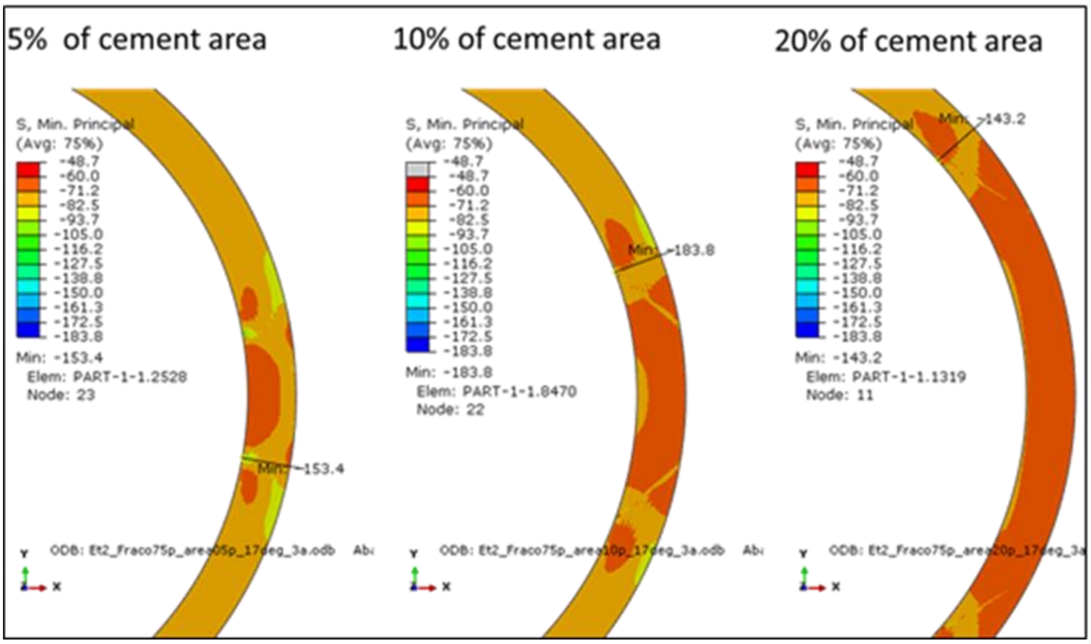

Figure 6-24: Maximum principal stress distribution for cement defects in Geometry No. 3.

Significant values of tension appear only for defected area sizes of 20 percent having a 75 percent reduction in parameters E, v and c. Within a few hours after it is introduced into the annular, the cement in Abaqus® exhibits tensile stress as it slowly decreases with time. According to Schlumberger's Oilfield Glossary, it takes approximately 12 to 24 hours for the cement to solidify in offshore oil wells. Tensile stress is taken into consideration strictly after a period of 24 hours to account for the event that the cement may not have hardened sufficiently in all spots. Since slurry as a fluid can only be under a hydrostatic state of stress, there will be no tensile stress nor shear stress within the solid cement (Gray et al., 2009). Geometry No. 2 shows tensile stress but no considerable values throughout the 28-day period for areas of 5 percent, 10 percent nor 20 percent. Geometry

No. 1 shows a magnitude greater than 15 MPa located on the upper corner on the casing-cement interface in 24 hours after the commencement of cementing. Given that in 24 hours a typical Class G cement gains a compressive strength of about 20 MPa (Carina, 2009) resulting in a tensile strength of nearly 2 MPa, any tension exceeding this value is significant and should be taken into consideration. It should be noticed that tensile stress appears strictly along the upper and lower boundaries of the defected cement region but nowhere else in the cement is tensile stress present. This corresponds to the 5 percent, 10 percent and 20 percent models for geometry No. 1, No. 2 and No. 3. Due to its steep corners, Geometry No. 3 presents the greatest tensile scenario as displayed in Figure 6-25.

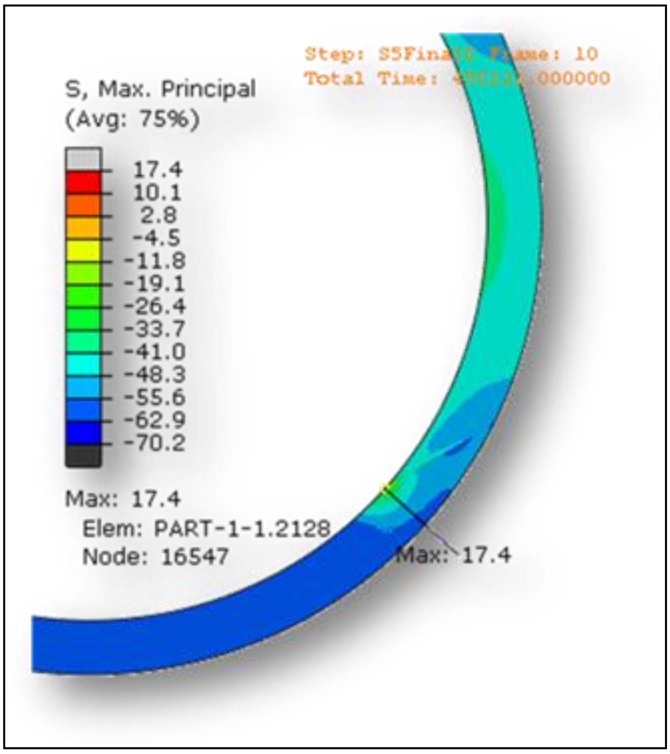

Figure 6-25: Tensile stress in the first 24 hours for Geometry No. 3 having a 20% defected area.

The cement defect was relocated 90 degrees from its current position for comparison. In view of Figure 6-26, the maximum compressive stress marginally decreases, but the stress distributed over the cement is shown to be greater for a cement defect along the axis of the OD_{max}. Therefore, a defect in the cement located on the same axis as the OD_{max} is more critical than if it were located perpendicular to the OD_{max}.

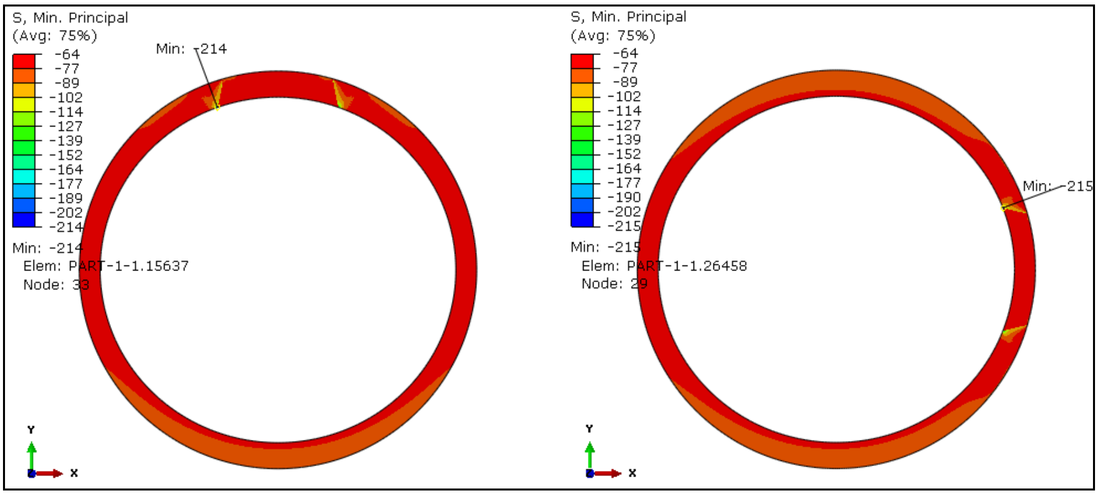

Figure 6-26: Left: Cement defect located perpendicular to the OD_{max}. Right: Cement defect along the same axis as the OD_{max}.

Ovalization proves to have a weighty effect upon the defected region's state of stress depending on its geometry. It can be seen in Figure 6-27 that an ovality of 1.5 percent reduces the maximum compressive stress in Geometry No. 1 nearly 28 percent. The maximum compressive stress in Geometry No. 2, however, drops insignificantly.

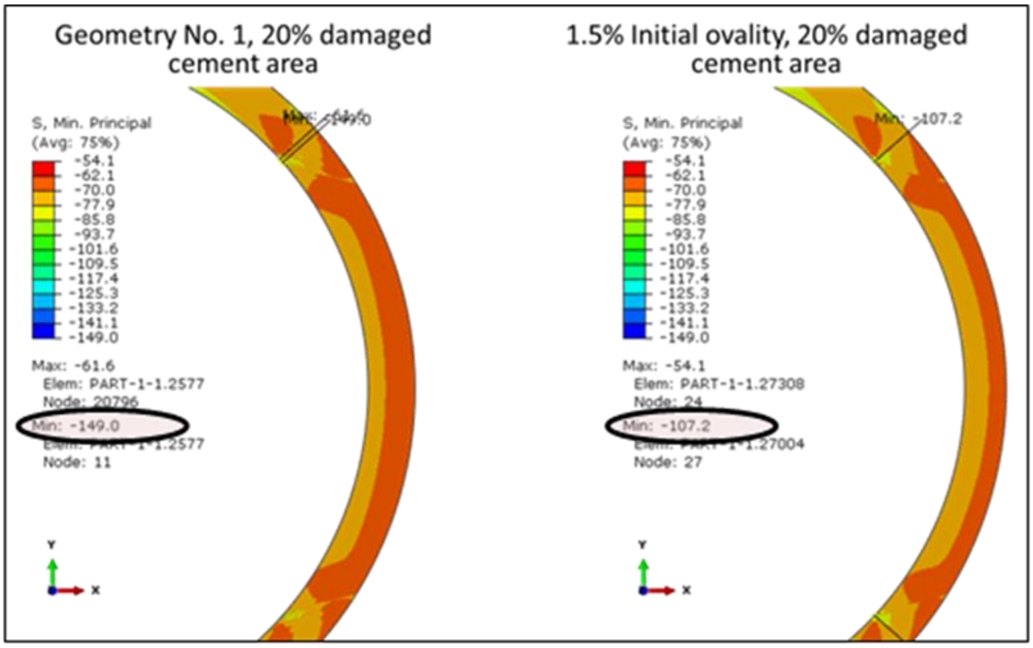

Figure 6-27: Comparison of maximum compressive stresses in Geometry No. 1, with and without ovality.

On the contrary, Figure 6-28 shows that ovalization augments the maximum compressive stress in Geometry No. 3. This is in fact due to the geometry's steep corner angles which encourage shearing.

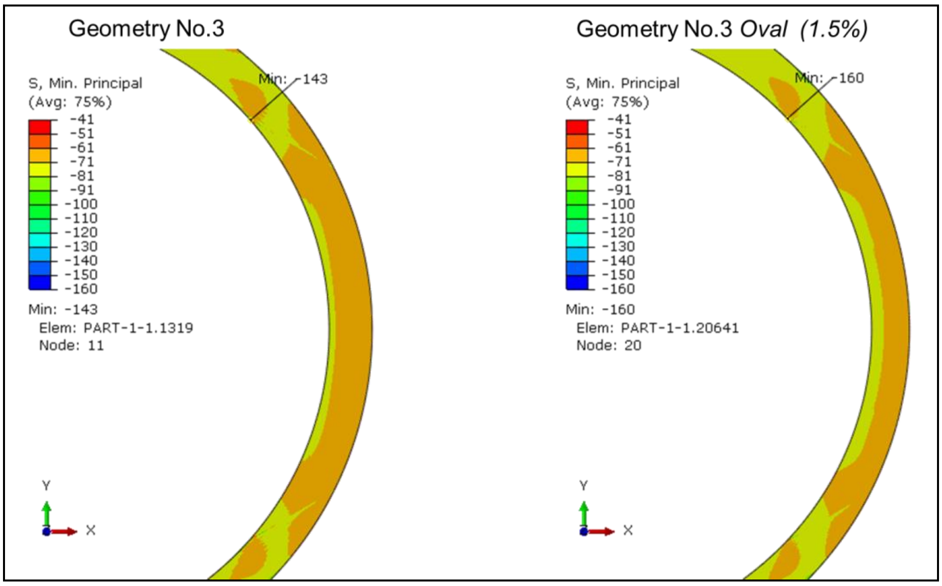

Figure 6-28: Geometry No. 3 with and without Ovalization (1.5%).

Ovalization also reduces tensile stress for nearly all of the geometries, and in fact, causes tension to vanish in Geometry No. 1 and No. 2. For Geometry No. 3, the tensile stress remains for the same reason mentioned previously for compressive stress (see Figure 6-29).

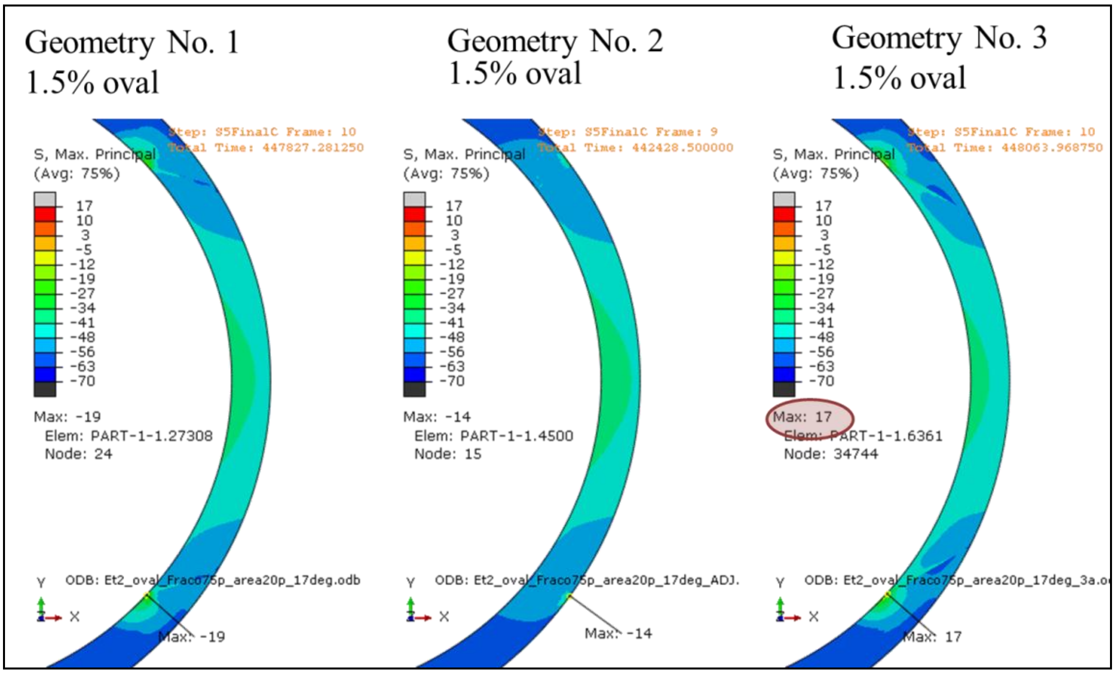

Figure 6-29: Compressive and tensile stress values for the three studied geometries.

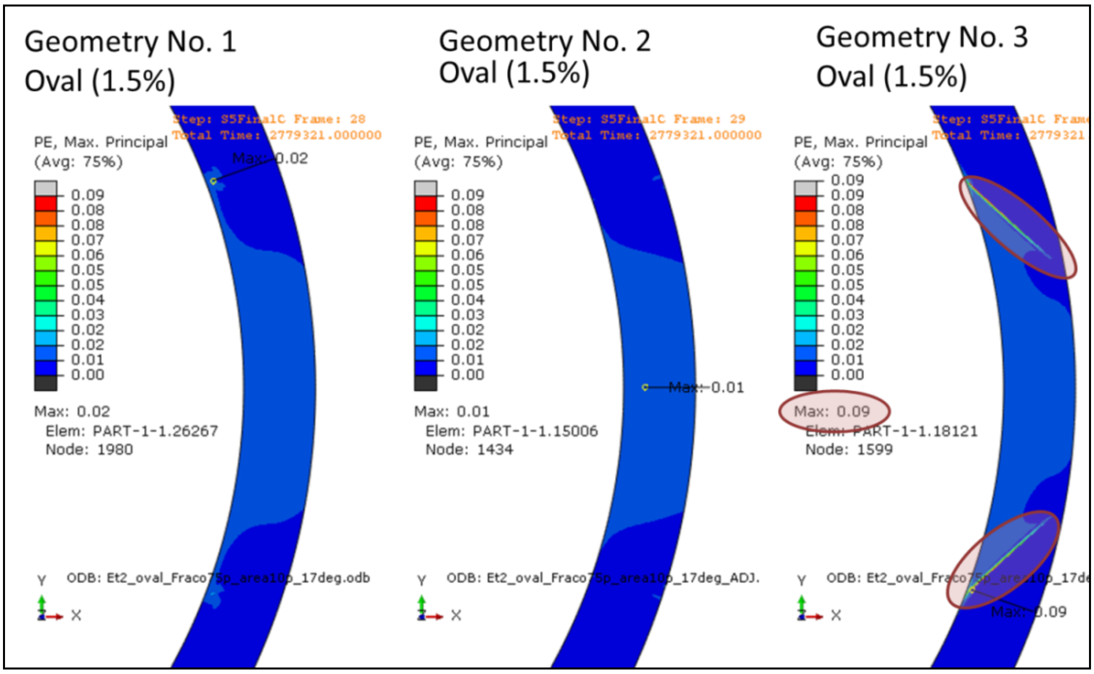

Figure 6-30: Plastic strain in the three geometries with 1.5% ovality.

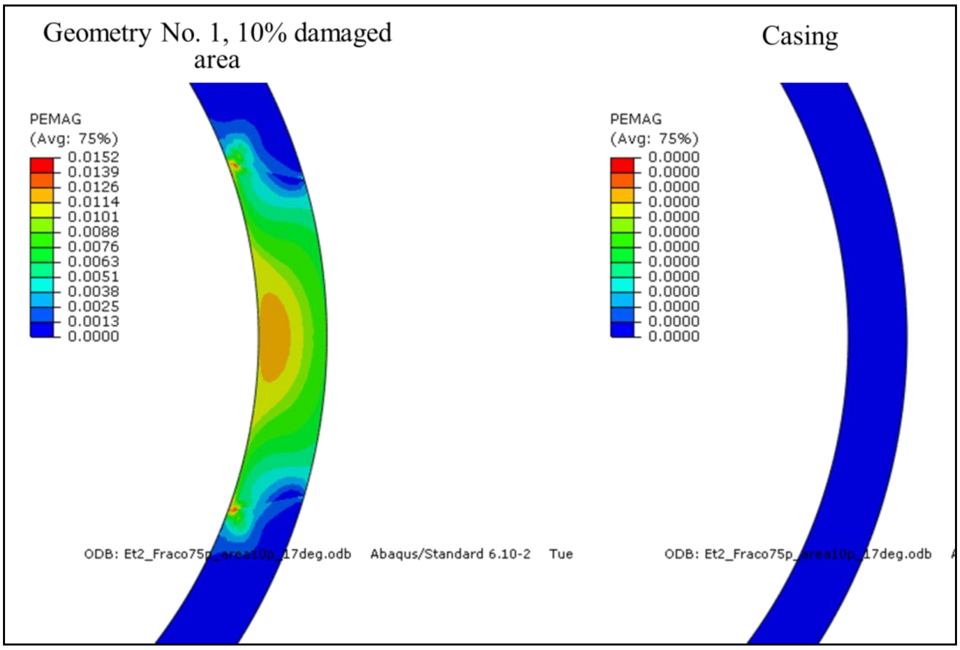

Figure 6-31: Plastic strain for the poorly-cemented region and non-oval casing.

Knowing the worst scenario, a further investigation was conducted to observe the state of stress in the cement and casing for Geometry No. 3 (1.5% ovality) after 60 days. Results in Table 6-15 and Table 6-16 show only a slight change in the cement and casing's stress conditions, increasing no more than two percent. In contrast with the results found in Stage 1, radial stress is dominant and controls plastic straining in the cement by the addition of the Mohr-Coulomb failure criterion. In the elastic model, there is no limit for the tangential stress, while in the elastic perfectly plastic model there exists a limit that the tangential stress cannot surpass. Also, the total strain increased up to 9 percent. The change in displacement is insignificant mostly because it includes wellbore closure along with the decrease in the cement area.

CEMENT	Geometry No. 3: 10% Poorly cemented with 1.5% ovality (φ = 17°, c = 5.25 MPa).				
E (MPa)	5,250	Stress	σ radial max.	σ tangential max.	Principal σ
ν	0.25	Mini graph	(MPa)	(MPa)	max.(MPa)
ε max:	9%		-199	-99	-200
u max (m):	0.02	Load Type:	comp.	comp.	comp.
CASING		**OD (y axis)**	**OD (x axis)**	**Ovalization**	
E (MPa)	210,000	**min (m)**	**max (m)**	(%)	
ν	0.28	3.50E-01	3.61E-01	1.51	
σyield (MPa)	758	Stress Mini graph	σ radial max. (MPa)	σ tangential max. (MPa)	Principal σ max. (MPa)
Mises (MPa):	214		-109	-294	-294
ε max:	0%	Load Type:	comp.	comp.	comp.
u max (m):	0				

CEMENT	Geometry No. 3: 10% Poorly cemented with 1.5% ovality (φ = 17°, c = 5.25 Mpa).				
E (MPa)	5,250	Stress	σ radial max.	σ tangential max.	Principal σ
ν	0.25	Mini graph	(MPa)	(MPa)	max.(MPa)
ε max:	9%		-197	-97	-198
u max (m):	0.02	Load Type:	comp.	comp.	comp.
CASING		**OD (y axis)**	**OD (x axis)**	**Ovalization**	
E (MPa)	210,000	**min**	**max**	(%)	
ν	0.28	3.50E-01	3.61E-01	1.50	
σyield (MPa)	758	Stress Mini graph	σ radial max. (MPa)	σ tangential max. (MPa)	Principal σ max. (MPa)
Mises (MPa):	206		-108	-291	-291
ε max:	0.05%	Load Type:	comp.	comp.	comp.
u max (m):	0				

Table 6-15: Comparison of 60-day results (top) with 28-day results (bottom) for Geometry No. 3.

CEMENT	60-day and 28-day cement comparison.	
60-day σ radial max. (MPa)	60-day σ tangential max. (MPa)	60-day Principal σ max.(MPa)
-199	-99	-200
1.0% greater	2.0% greater	1.0% greater
CASING	60-day and 28-day casing comparison.	
60-day σ radial max. (MPa)	60-day σ tangential max. (MPa)	60-day Principal σ max. (MPa)
-109	-294	-294
0.9% greater	1.0% greater	1.0% greater

Table 6-16: 60-day comparison with 28-day results (1.5% ovality) for Geometry No. 3.

In summary, Geometry No. 1 is affected mostly by ovalization while Geometry No. 2 overall shows the lowest maximum stress values and Geometry No. 3 exhibits the greatest maximum stresses. For all scenarios, plastic straining in the cement is dominantly controlled by compressive stress while tensile stress plays a stronger role in Geometry No. 3. Plastic straining never occurs in the casing (See Figure 6-31). Furthermore, it displays values of von Mises stress no greater than 50 percent of the SMYS (758 MPa) in all scenarios. Hence, it is acceptable to simulate the casing as elastic.

6.9.5
Stage 3: Eccentricity

A major part of this research is simulating poorly-cemented casing when it is eccentric to the wellbore. Eccentricity and poor cementing are the two main contributors of non-uniform loading upon the casing (Salehabadi, 2011 and Shen, 2011). In addition, salt creep enhances the non-uniform loading by closing the wellbore over time. This leaves less spacing in the annular for the cement to distribute itself evenly and attain good quality. As was mentioned in chapter 5.1.1, eccentricity is defined as the ratio between the casing deviation to the annulus width at the time of cement displacement. Observing the results obtained from Stage 2, the deformed distance between the salt rock and the casing's exterior surface decreases to 2.4 cm. This distance will also be referred to as the *annular spacing*. Small spacing alone creates a critical scenario. Hence this leaves little room for the casing to translate, but it was hypothesized that eccentricity could still have an impact in these situations. It is sensible to simulate casings with a high eccentricity such as 90 percent demonstrated by Berger et al. (2004) since a small eccentricity would be meaningless in these circumstances. Knowing the annular spacing and also choosing an appropriate eccentricity percentage, the casing's deviation δ can be found:

$$Eccentricity\% = \frac{\delta}{R_w - r_c} \cdot 100$$

For 90% eccentricity, δ ~ 2.16 cm

The casing was shifted horizontally to the right by the distance δ where the same scenarios from Stage 2 would be simulated.

6.9.6
Stage 3: Results for Eccentricity

The goal of simulating the casing with 90 percent eccentricity was not successfully simulated in Abaqus®. Node rearrangement was very large in which the nodes would, for instance, surpass the displacement of the node lying in front of it pertaining to the same element (see Figure 6-32 below) or shared by elements. This resulted in negative eigenvalues in which remeshing was required.

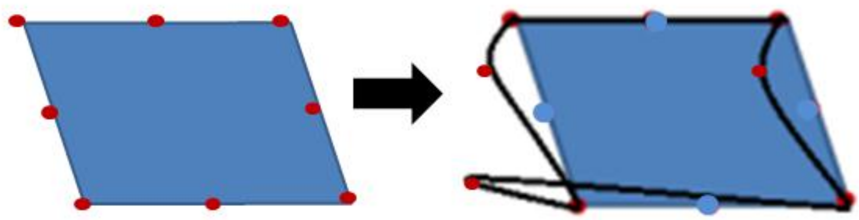

Figure 6-32: Excessively distorted 8-node quadrilateral element.

The discrepancy was resolved by increasing the element sizes for the cement mesh combined with a slight reduction in eccentricity to 85 percent:

$$85\% = \frac{\delta}{2.4cm}100$$

$$\delta \approx 2.0cm$$

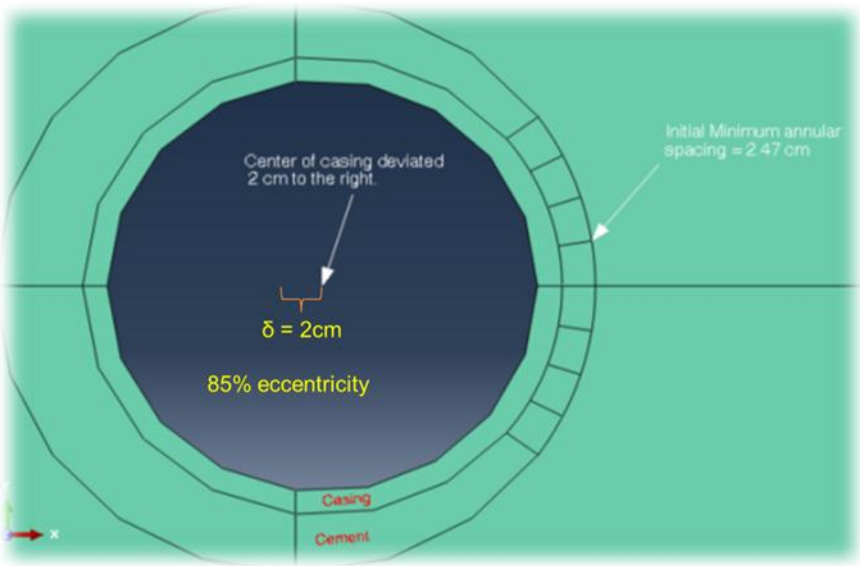

Figure 6-33 Abaqus sketch of the eccentric casing.

The results show cement failure to be controlled by compression as was determined in the previous section for simulations having no eccentricity. Figures 6-34 and 6-35 respectively show the radial stresses and tangential stresses induced by the salt formation immediately after cementing, validating the presence of non-uniform loading.

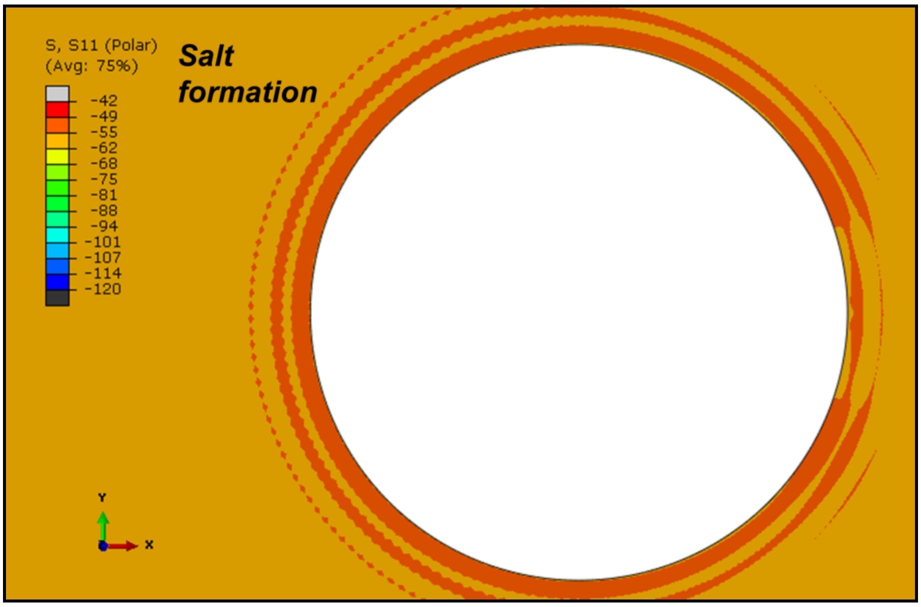

Figure 6-34: Non-uniform radial stress distribution induced by salt formation immediately after cementing (casing and cement not displayed).

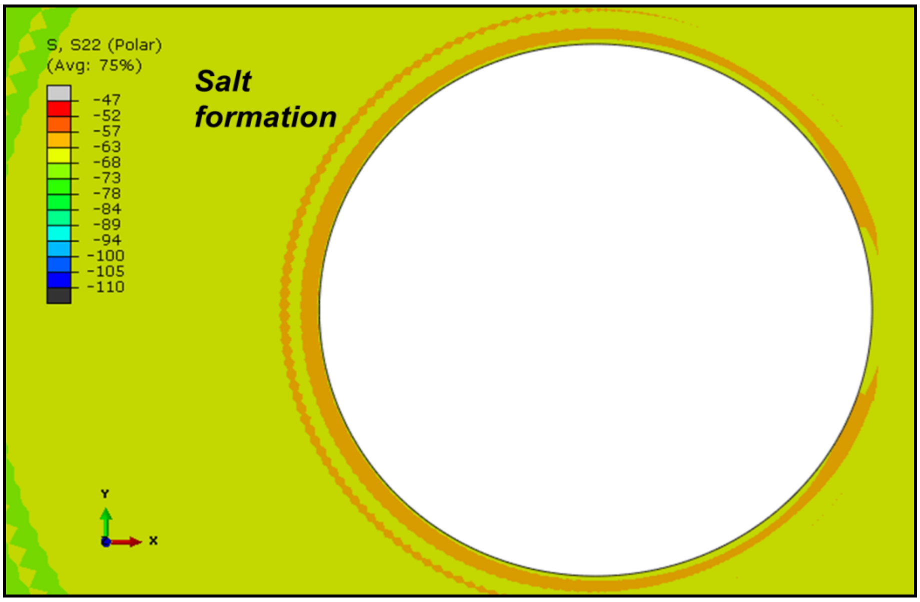

Figure 6-35: Non-uniform tangential stress distribution induced by salt formation immediately after cementing (casing and cement not displayed).

Results also indicate that the size of the defected area becomes less sensitive due to eccentricity. With eccentricity, the values of compressive stress vary little with respect to the defected sizes for both 15 percent and 75 percent reductions of parameters E, v and c. On the contrary, Geometry No. 2 with eccentricity shows an increase in maximum compressive stress of almost 9 percent (see Figure 6-36). Its geometry initially has flat boundary edges; however the small annular spacing provoked by eccentricity causes the midpoint of its extremities to protrude, creating arrow-shaped edges. Such geometry portrays greater stress than geometries with sharp-cornered edges such as Geometry No. 1 and No. 3 since the latter geometries are more susceptible to failure. With the exception of Geometry No. 2, it can be concluded that the smaller the cement-filled annulur spacing is, the less control the geometry of the defected area has on the cement's strength and failure. Confirmed by similar studies (Akgun et al., 2004), the analyses results indicate that the critical cement region for eccentric casings is almost guaranteed to be located in the area having the smallest annular spacing.

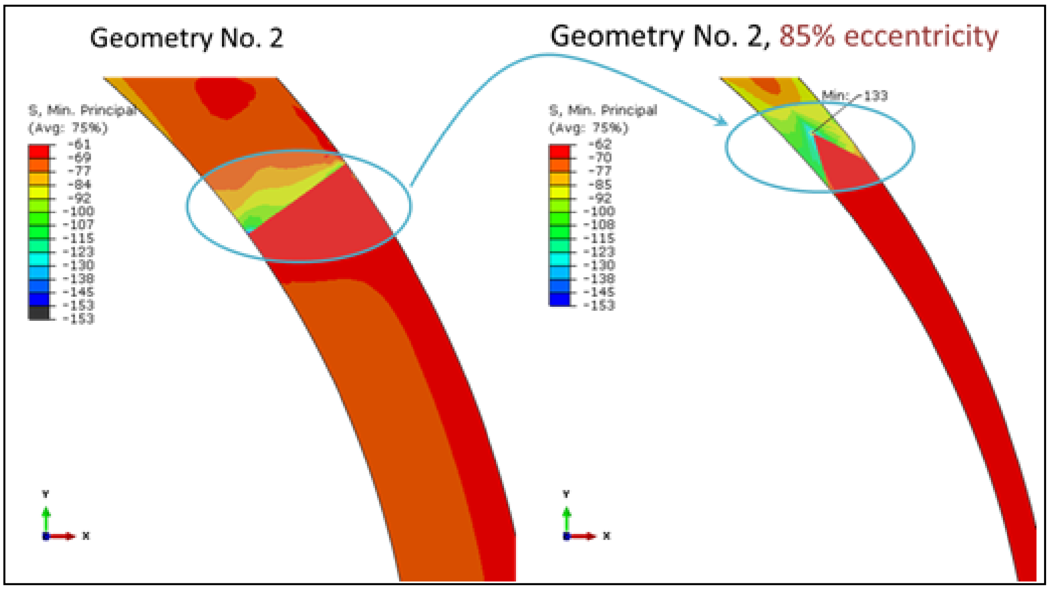

Figure 6-36: Effects upon the boundary in Geometry No. 2 due to eccentricity.

All of the eccentricity simulations exhibit no significant tensile stress. This is primarily due to the compressive stress from salt creep. Hence, cement failure continues to be controlled by compression. Comparing models with 15 percent and 75 percent parameter reductions for an area size of 10%, the maximum principal compressive stress for the latter is nearly 88 percent greater than for the 15 percent parameter reduction. In spite of plasticity, all three geometries yielded results that were quite similar. With a 15 percent reduction in E, v and c, plastic strain appears solely near the upper and lower boundaries of the defected cement region while its core shows no plastic strain. This is also due to well closure provoked by salt creep, where the annular achieves an unbalanced geometry that leaves little spacing for cement filling. As a result, the non-uniform salt loading squeezes the cement through the annular area with little spacing and begins to fail along its extremities.

Ovality reduces the compressive stress upon the cement by no more than 3 percent as shown in Figure 6-37. Furthermore, it leaves less room for the cement filling in the defected region (i.e., considering that the casing translates along the same axis of the maximum OD). Overall, casing ovalization increases the risk of poor cement jobs including weak cementation, voids or channels if casing eccentricity exists.

In terms of geometry, there is virtually no difference in compressive stress when comparing circular casings and ovalized casings with the exception of Geometry No. 2. Similar to results from Stage 2, the greatest values of compressive stress are found along the upper and lower boundaries within the poorly-cemented area regardless of geometry or size. Although a concentric casing with Geometry No. 2 may portray a higher maximum compressive stress value in the cement, eccentricity creates a larger stress zone with higher magnitudes surrounding the boundaries of the defected cement (see Figure 6-38). Casing eccentricity therefore increases the possibility of cement failure due to compressive stress in salt formations, knowing that compressive stress depends upon the defected cement's geometry.

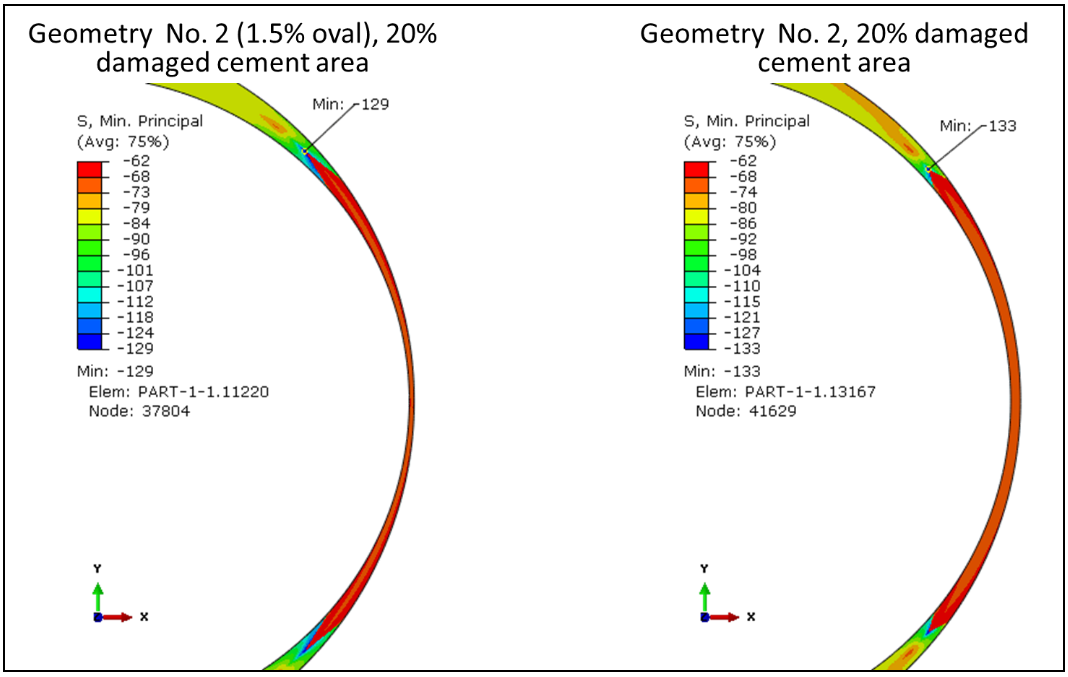

Figure 6-37: Comparison of the maximum compressive stress in Geometry No. 2.

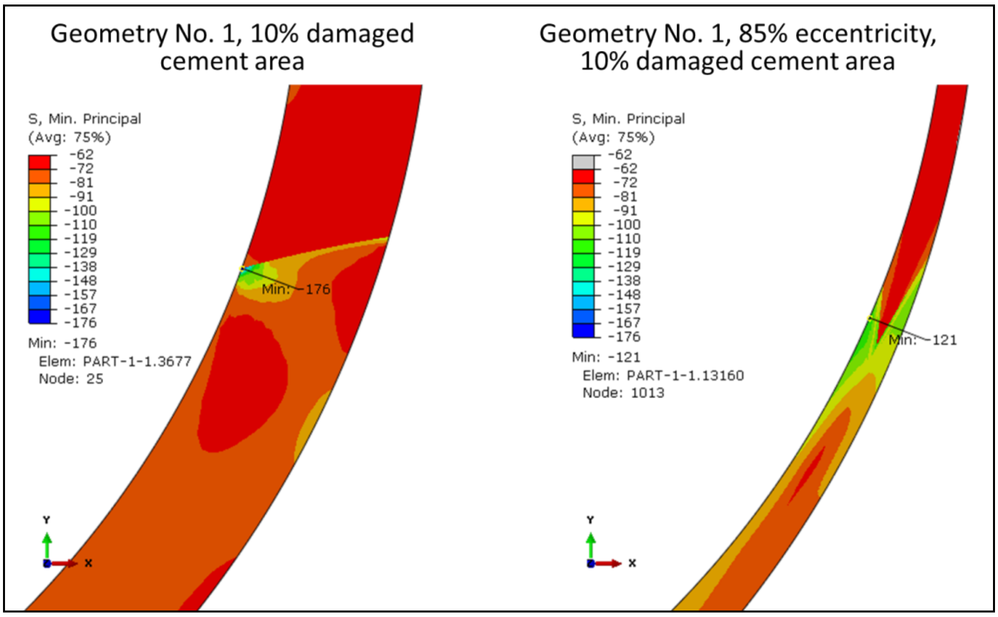

Figure 6-38: Comparison of the maximum compressive stress for Geometry No.1.

As for Geometry No. 3, accurate eccentricity results could not initially be retrieved. With its steep angles combined with the thin annular space for meshing provoked negative eigenvalues to appear during simulation. An approach was taken to estimate the output stress values for an 85 percent eccentricity scenario. The results from Geometry No. 2 show a difference between a 33 percent eccentric and 85 percent eccentric casing in terms of compressive stress of approximately 13 percent. This correlation was used to estimate the results for Geometry No. 3. Having a 33 percent eccentric casing successfully simulated for Geometry No. 3, its compressive stress values for an 85% eccentric casing were extrapolated by reducing the stresses by 13 percent as seen in Figure 6-39. As for tensile stress, no significant change was found by extrapolation. Consequently, Geometry No. 3 is practically the most unfavorable of all three geometries.

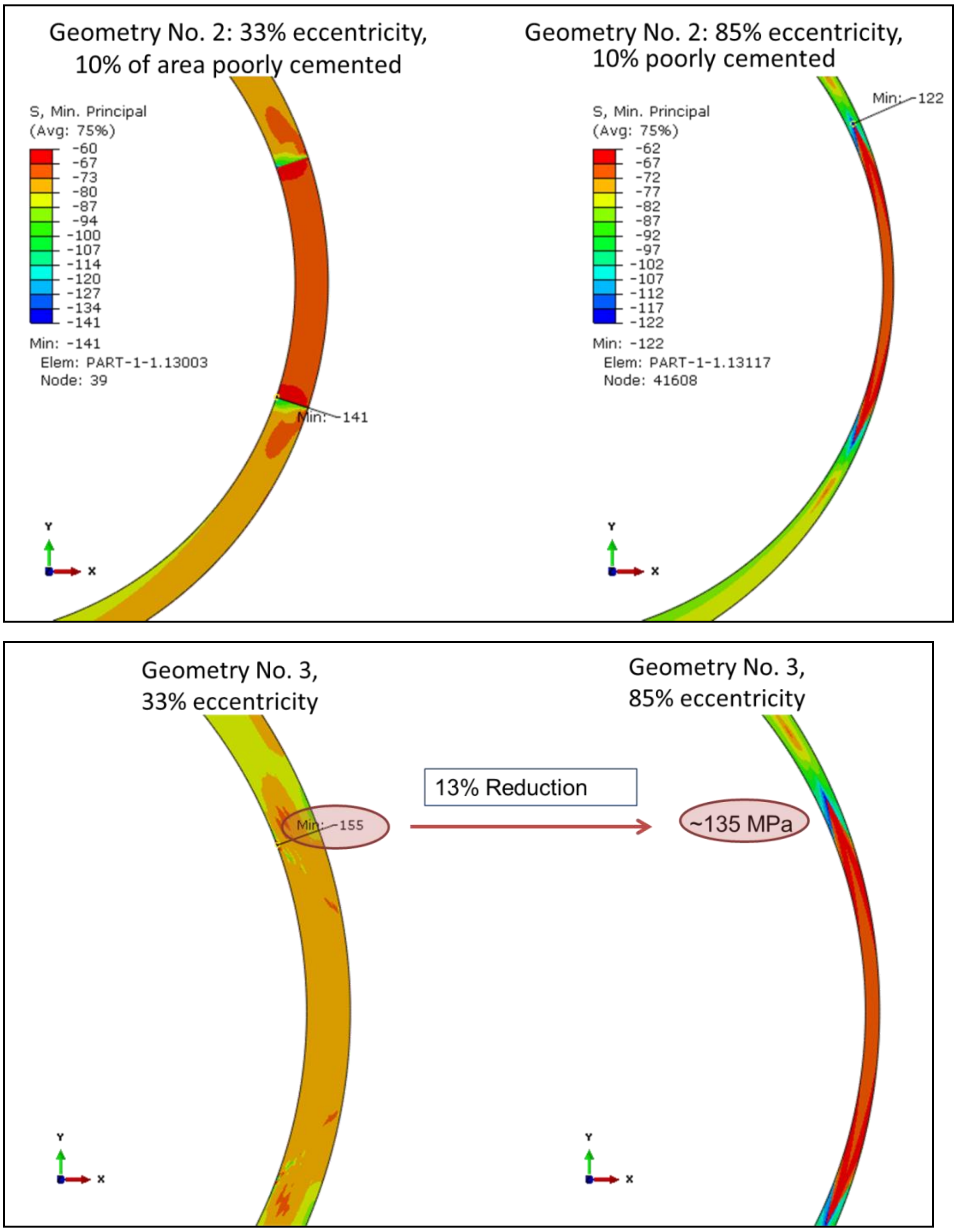

Figure 6-39: Top: An estimate was made for Geometry No. 3 using data from Geometry No. 2. Bottom: A 13% difference in compressive stress was used to extrapolate the approximate value.